

Constraints on Explosion Timescale of Core-Collapse Supernovae Based on Systematic Analysis of Light Curves

SEI SAITO,¹ MASAOMI TANAKA,^{1,2} RYO SAWADA ,³ AND TAKASHI J. MORIYA ^{4,5}

¹*Astronomical Institute, Tohoku University, Sendai 980-8578, Japan*

²*Division for the Establishment of Frontier Sciences, Organization for Advanced Studies, Tohoku University, Sendai 980-8577, Japan*

³*Department of Earth Science and Astronomy, Graduate School of Arts and Sciences, The University of Tokyo, Tokyo 153-8902, Japan*

⁴*Division of Science, National Astronomical Observatory of Japan, National Institutes of Natural Sciences, 2-21-1 Osawa, Mitaka, Tokyo 181-8588, Japan*

⁵*School of Physics and Astronomy, Faculty of Science, Monash University, Clayton, Victoria 2800, Australia*

ABSTRACT

Explosion mechanism of core-collapse supernovae is not fully understood yet. In this work, we give constraints on the explosion timescale based on ^{56}Ni synthesized by supernova explosions. First, we systematically analyze multi-band light curves of 82 stripped-envelope supernovae (SESNe) to obtain bolometric light curves, which is among the largest samples of the bolometric light curves of SESNe derived from the multi-band spectral energy distribution. We measure the decline timescale and the peak luminosity of the light curves and estimate the ejecta mass (M_{ej}) and ^{56}Ni mass (M_{Ni}) to connect the observed properties with the explosion physics. We then carry out one-dimensional hydrodynamics and nucleosynthesis calculations, varying the progenitor mass and the explosion timescale. From the calculations, we show that the maximum ^{56}Ni mass that ^{56}Ni -powered SNe can reach is expressed as $M_{\text{Ni}} \lesssim 0.2 M_{\text{ej}}$. Comparing the results from the observations and the calculations, we show that the explosion timescale shorter than 0.3 sec explains the synthesized ^{56}Ni mass of the majority of the SESNe.

Keywords: supernovae: general

1. INTRODUCTION

Massive stars whose initial masses are $\gtrsim 8 M_{\odot}$ explode at the end of their lives as core-collapse supernovae (CCSNe). After the core collapses, the central density increases, which eventually stops the core contraction. This causes a bounce of the core, generating a shock wave. If the shock wave propagates to the surface of the star, the supernova (SN) explosion is considered to be successful. However, the explosion mechanism of CC-SNe is not fully understood yet. The propagation of the shock wave is halted by endothermic reactions due to photodisintegration of iron and by ram pressure of falling materials from the outer part. Successful explosions thus require a mechanism to revive the shock wave. The most plausible mechanism is a neutrino-driven explosion mechanism (Arnett 1966; Colgate & White 1966;

Bethe & Wilson 1985). In this mechanism, part of the neutrinos produced in the dense core are absorbed by materials behind the shock wave, reviving the shock wave. As a result, the SN explosion driven by neutrinos can occur.

It has been known that in multi-dimensional ab-initio calculations with the neutrino-driven explosion mechanism (e.g., Janka 2012; Takiwaki et al. 2014; Lentz et al. 2015; Melson et al. 2015b,a; Müller et al. 2017, 2019; Ott et al. 2018; Summa et al. 2018; Burrows et al. 2019, 2020; Stockinger et al. 2020), the kinetic energy only reaches $E_{\text{k}} \sim 10^{50}$ erg, while a typical energy estimated from observations is $E_{\text{k}} \sim 10^{51}$ erg (e.g., Hamuy 2003; Drout et al. 2011; Cano 2013; Pejcha & Prieto 2015; Taddia et al. 2015, 2018; Lyman et al. 2016; Barbarino et al. 2021). Some of recent simulations have been reported to reach $E_{\text{k}} = 10^{51}$ erg (e.g., Burrows & Vartanyan 2021; Bollig et al. 2021), and the problem in the explosion energy is gradually being solved. It should be noted, however, that many simulations do not repro-

duce energetic explosion. Moreover, the timescales to reach the sufficient kinetic energy in those calculations are ~ 1 sec or even longer.

Such a slow explosion tends to result in a relatively small production of ^{56}Ni ($\sim 0.03 M_{\odot}$; e.g., Müller et al. 2017), which is a radioactive nucleus powering SNe by the radioactive decay through ^{56}Co to ^{56}Fe (Arnett 1966). In models with calibrated neutrino luminosity to reproduce SN explosions, the synthesized ^{56}Ni mass can be $\lesssim 0.1 M_{\odot}$ (e.g., Ugliano et al. 2012; Ertl et al. 2020; Woosley et al. 2021), which is higher than that from ab-initio calculations.

The ^{56}Ni mass has been estimated from observations. For stripped-envelope SNe (SESNe; Type IIb, Ib, Ic, and Ic BL (standing for broad line)) without hydrogen-rich envelopes, the ^{56}Ni mass is often estimated from the peak of their light curves based on a semi-analytic model (Arnett’s rule; Arnett 1982). The range of the mass is $\sim 0.0015 M_{\odot} - \sim 1 M_{\odot}$ with the median value of $\sim 0.15 M_{\odot}$ (Anderson 2019; Meza & Anderson 2020). On the other hand, for Type II SNe with hydrogen-rich envelopes, the ^{56}Ni mass is estimated from the tail of their light curves (from the ^{56}Co decay, e.g., Woosley 1988). The range of the mass is $\sim 0.001 M_{\odot} - \sim 0.3 M_{\odot}$ with the median value of $\sim 0.03 M_{\odot}$ (Anderson 2019; Meza & Anderson 2020). It should be noted, however, that lack of the ^{56}Ni mass in the lower side of SESNe can be explained by observation bias (Ouchi et al. 2021).

These observational facts imply that the range of the ^{56}Ni mass estimated from observations cannot easily be explained by ab-initio calculations nor models with calibrated-neutrino luminosity. For example, Sollerman et al. (2021) compared the peak luminosities of many observed SESNe in optical bands with those expected from the models with calibrated neutrino luminosity (Woosley et al. 2021). They have shown that only ~ 60 % of the luminosities of the observed SESNe can be reproduced by the model.

To understand the necessary condition of CCSNe, several works have been done based on “artificial-explosion” calculations (e.g., Maeda & Tominaga 2009; Suwa & Tominaga 2015; Suwa et al. 2019). Those studies have pointed out that the synthesized ^{56}Ni mass increases with the decrease of the explosion timescale.

While the explosion timescale of $\gtrsim 1$ sec (“slow” explosions) has been predicted by the current ab-initio calculations, Sawada & Maeda (2019) has shown that the shorter explosion timescale of $\lesssim 0.25$ sec (“rapid” explosions) is required to reproduce the typical mass of ^{56}Ni . However, they did not compare their results with concrete observational data and only showed a general trend in comparison with some progenitors of typical

SNe. Here, various progenitors, together with various explosion timescales, should be considered to estimate ^{56}Ni mass because the production of ^{56}Ni depends not only on the explosion timescale but also on progenitor stars (e.g., Woosley & Weaver 1995; Sukhbold et al. 2016).

In this work, we compare ^{56}Ni masses estimated from observations and from calculations varying progenitor stars. We perform the systematic analysis of observed light curves of SESNe including Type I superluminous supernovae (Type I SLSNe or SLSNe-I; hydrogen-poor SLSNe) whose peak magnitudes are $\lesssim -21$ mag (e.g., Gal-Yam 2012; Moriya et al. 2018; Nicholl 2021). Although the high luminosity of SLSNe is difficult to be explained by ^{56}Ni , it is not clear up to what luminosity radioactive decay of ^{56}Ni can serve as a power source.

This paper is organized as follows. Section 2 describes methods to systematically analyze multi-band light curves of SESNe to estimate the synthesized the ^{56}Ni mass with the maximum sample number to date. Section 3 shows the results of the systematic analysis of the light curves. In Section 4, we carry out one-dimensional hydrodynamics and nucleosynthesis calculations to investigate the synthesized ^{56}Ni mass. Furthermore, we discuss the maximum luminosity of ^{56}Ni -powered SNe and the explosion timescale of CCSNe. Finally, the conclusions are given in Section 5.

2. DATA SELECTION AND ANALYSIS

In this section, we describe observational data used in our analysis and methods of the analysis. We derive bolometric light curves of 82 SESNe from the multi-band observational data and measure decline timescales and peak magnitudes from the bolometric light curves. The sample selection and the procedure of the analysis are shown in Figure 1.

2.1. Types of supernovae

We used photometric data of SNe from a SN database, Open Supernova Catalog (Guillochon et al. 2017). The catalog has 59603 objects as of 2020 Mar 13, including 5212 CCSNe. We selected SESNe including SLSNe-I from the sample, finding 820 SESNe. The reason why we only selected SESNe is that their ^{56}Ni mass can be estimated from the peak luminosity. Furthermore, we can estimate the ejecta mass from the light curve, which provides the connection with the progenitor stars.

2.2. Interpolation of photometric data

We smoothly connect the data points of the SESNe selected in the previous section to interpolate the data points, which are inevitably caused by intervals of observations. To ensure the reliable interpolation, we only

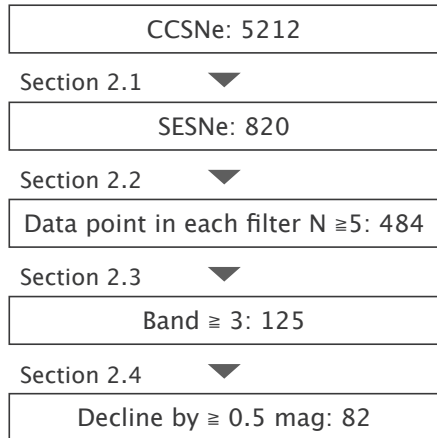


Figure 1. The procedure to select our sample with the section number and the number of the sample.

use the data with the observational points $N \geq 5$ for each filter. After this criterion, 484 SNe remain.

For the interpolation of data points, we performed Gaussian Process Regressions (GPRs), which can express complex nonlinear functions by superposition of infinite number of functions. The kernel of the GPR used for fitting is *constant* \times Radial Basis Functions. The kernel length parameter is fitted to obtain the best match with the data. Figure 2 shows a comparison of data before the GPR and after the GPR, demonstrating that the observational data points are smoothly fitted with the GPR.

Here, we discuss some light curves which we manually eliminated from our data analysis. Some light curves cannot be fitted well by the GPR method due to the sparseness of data points. The eliminated light curves of SNe and bands are following. PS16yj: *UVM2*; PS1-12sk: *UVW1, UVW2, UVM2*; PTF09cnd: *UVW1, UVW2, UVM2*; PTF12dam: *UVW1, UVW2, U, i*; SN 2004dk: *I*; SN 2005az: *R, r*; SN 2007Y: *U*; SN 2009jf: *u, i*; SN 2009mg: *UVW1*; SN 2010bh: *B*; SN 2011kg: *UVW1, UVW2, u, U*; SN 2013hy: *g*; SN 2014ad: *UVW1, UVW2, UVM2*; SN 2015bn: *V, i, z*; SN 2016coi: *U, I*; SN 2017ein: *I*; iPTF13bvn: *UVW2, U*.

2.3. Bolometric light curve

We here derive bolometric light curves using multi-band light curves obtained above. First, we correct the dust extinction. Then, we take the luminosity distances d_L to obtain the absolute magnitudes. After that, we perform blackbody fitting to derive bolometric light curves. In our analysis, the Vega magnitudes have been converted to the AB magnitudes based on Blanton & Roweis (2007).

The extinction of the Milky Way was corrected based on the dust map estimated in Schlegel et al. (1998). On the other hand, the extinction of host galaxies of SNe was not corrected since the degree of host extinction is uncertain. It is noted that although the typical value of host extinction is $A_V \sim 0.6$ for Type IIb and Ib SNe and $A_V \sim 1$ for Type Ic SNe (Stritzinger et al. 2018) or $A_V \sim 0.9$ for SESNe (Zheng et al. 2022), ignoring the host extinction does not affect on the conclusion of this work. This is because we will use the upper limit of the luminosity in our discussion (Section 4.2).

To obtain the absolute magnitudes, we took the luminosity distances d_L from Open Supernova Catalog. For the distances for which the method of the estimate is uncertain, we instead used the distances based on the Cepheid measurement ($\lesssim 10$ Mpc), the Tully Fisher relation ($\sim 10 - \sim 20$ Mpc Tully & Fisher 1977), and the redshift with a correction from Galactic infall model ($\gtrsim 20$ Mpc). Figure 3 represents a relation between luminosity distances and peak absolute magnitudes in the band that shows the maximum brightness among all the bands used for each object. The luminosity distances d_L are mainly in the range of $10 \lesssim d_L \lesssim 1000$ Mpc and the peak magnitudes range from -14 to -24 mag. More luminous objects tend to be observed at larger distances due to the observational bias.

To derive bolometric luminosities, we performed the blackbody fitting to the spectral energy distributions (SEDs) estimated with the methods in Section 2.2 if a SN was observed with ≥ 3 bands. The spectra can be approximated with a blackbody (e.g., Modjaz et al. 2009) because SNe in photospheric phases mainly have thermal radiation typically until ~ 50 days after the explosion. Figure 4 shows an example of SEDs with the time evolution. The SEDs are approximated well with a blackbody radiation until 50 days after the explosion. By integrating the fitted flux over the entire wavelength, we have obtained bolometric light curves of 125 SNe.

2.4. Measurement of decline timescale and peak magnitude

From the bolometric light curves constructed in Section 2.3, we measure peak bolometric absolute magnitudes M_{peak} and decline timescales $\Delta t_{0.5\text{mag}}$. Here, $\Delta t_{0.5\text{mag}}$ is defined as the time it takes for the light curve to decline by 0.5 mag from the peak luminosity, which is the time for the light curve to decline by 0.5 mag from the peak. We finally measured the peak absolute magnitudes and the decline timescales of 82 SNe. The sample consists of 14 SLSNe-I, 13 Type IIb, 21 Type Ib, 24 Type Ic, 6 Type Ic-BL and 4 Type Ibc.

3. RESULTS

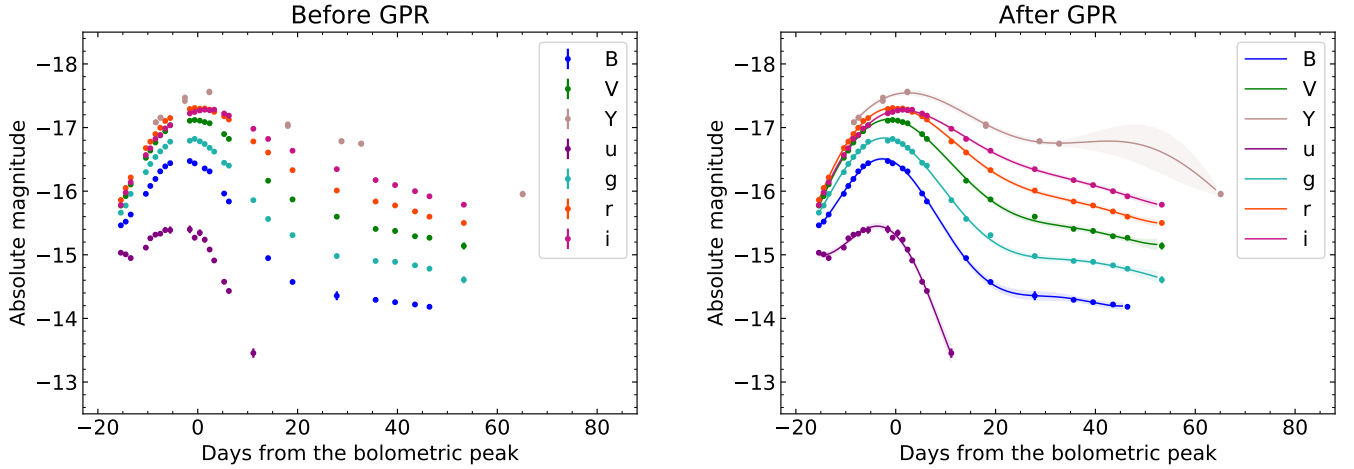


Figure 2. An example of multi-band light curves before (the left panel) and after (the right panel) the GPR (Type IIb SN 2004ex). The different colors show different bands as shown in the legend.

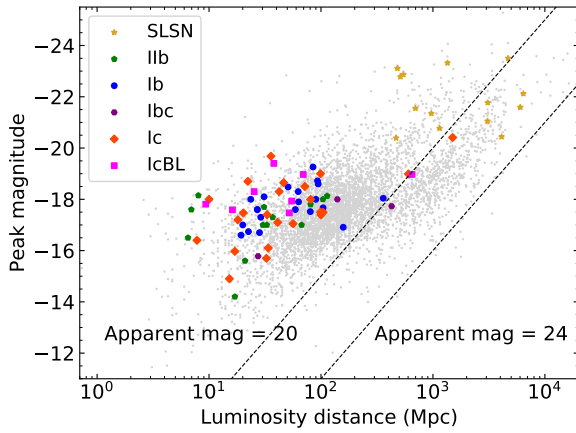


Figure 3. A relation between luminosity distances and peak absolute magnitudes in the band that shows the maximum brightness among all the bands used for each object. The gray points show all the CCSNe in Open Supernova Catalog, and the colored points show our final samples. The different colors represent different types of SNe as shown in the legend. Note that the peak magnitudes are different from the bolometric magnitudes in Figure 6.

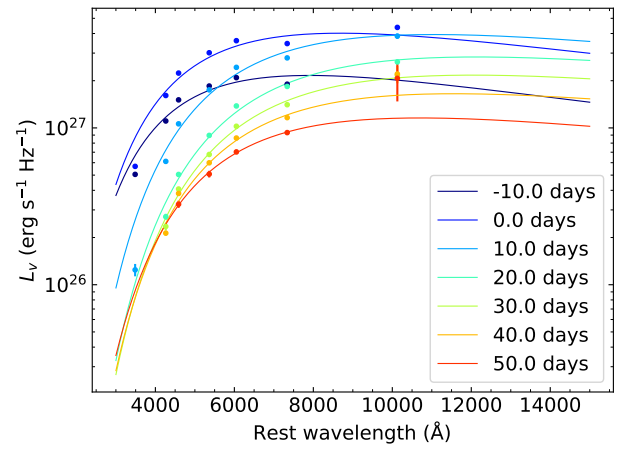


Figure 4. An example of time evolution of SEDs (SN 2004ex). The different colors show different epochs in the rest frame from the bolometric peak luminosity, as shown in the legend.

3.1. $\Delta t_{0.5\text{mag}}$ vs. M_{peak}

Figure 5 shows the bolometric light curves of the 82 SNe derived with the methods described in Section 2.

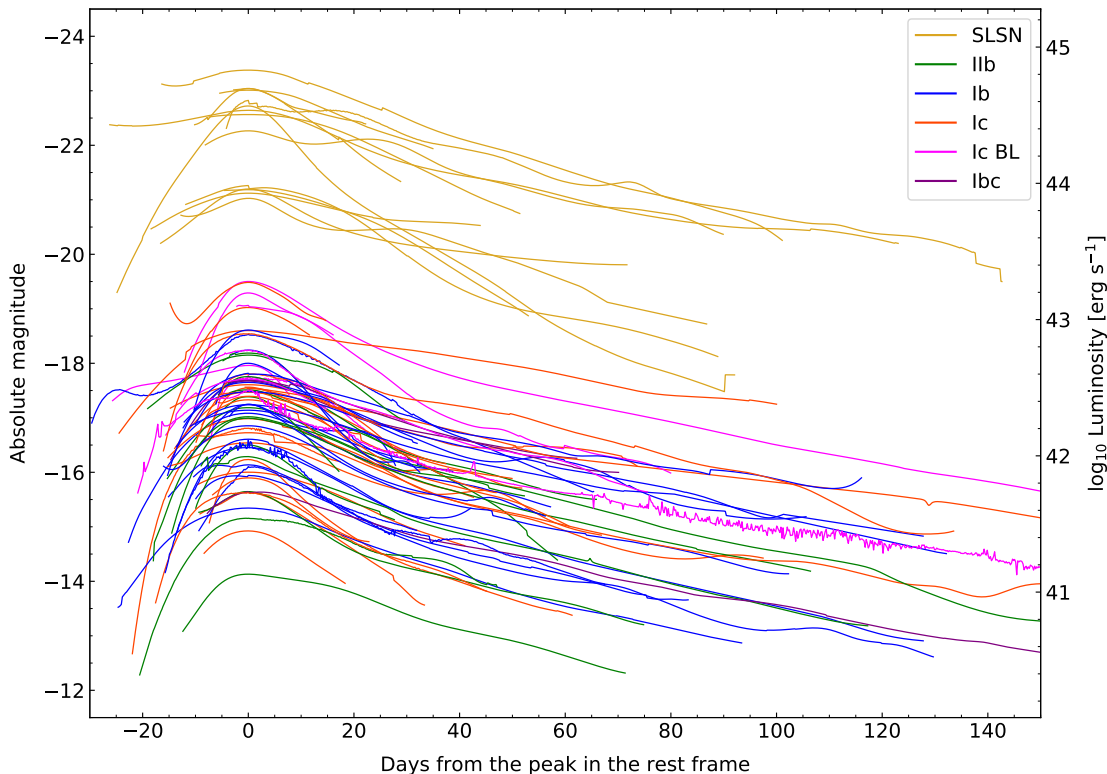


Figure 5. Bolometric light curves of our samples. The different colors show different types of SNe as shown in the legend.

The light curves have a variety of peak luminosities and time evolutions. Some sharp features in the bolometric light curves are due to the variation in the number of data points used in the SED fitting: when the number of bands changes, the best fit blackbody parameters can significantly vary, causing the sharp features. From the bolometric light curves, we estimate the decline timescales $\Delta t_{0.5\text{mag}}$ and the peak bolometric magnitudes M_{peak} (Table 6). Figure 6 represents a relation between $\Delta t_{0.5\text{mag}}$ and M_{peak} .

The distribution of the decline timescales is concentrated from ~ 10 days to ~ 20 days. On the other hand, the distribution of the peak magnitudes is broad, from ~ -14 mag to ~ -24 mag. All the SNe classified as SLSNe in the database are more luminous than -21 mag as expected from the definition.

It is noted that the distribution of the absolute magnitudes does not reflect the true distribution of SNe since more luminous SNe have a bias to be observed more easily. Also, although there seems a gap of the distribution, that is, less objects are located in around -20 mag, it can also be considered as a bias that extremely luminous objects with the peak magnitudes $\lesssim -21$ tend to

get more attention for follow-up observations. In fact, previous systematic studies show that there is no gap in the luminosity distribution between normal SNe and SLSNe (Arcavi et al. 2016; De Cia et al. 2018; Perley et al. 2020; Prentice et al. 2021).

Also, there is no clear correlation between the decline timescales and the peak magnitudes showing a correlation coefficient of 0.07 without the SLSNe. Furthermore, their distributions are not clearly different among Type IIb, Ib, and Ic SNe, as shown in the cumulative distributions of $\Delta t_{0.5\text{mag}}$ and M_{peak} of Figure 6. P-values of $\Delta t_{0.5\text{mag}}$ and M_{peak} from K-S tests for Type IIb vs. Ib SNe, Type Ib vs. Ic SNe, and Type Ic vs. IIb SNe are summarized in Table 1. This indicates that their distributions are not distinguishable.

3.2. M_{ej} vs. M_{Ni}

We estimate the ejecta mass M_{ej} and the ^{56}Ni mass from the decline timescale $\Delta t_{0.5\text{mag}}$ and the peak magnitude M_{peak} , respectively, using the semi-analytic model (Arnett 1982). Although we can also use, for example, $\Delta t_{1\text{mag}}$, which is the time for the light curve to decline by 1 mag from the peak, to estimate the ejecta mass, we

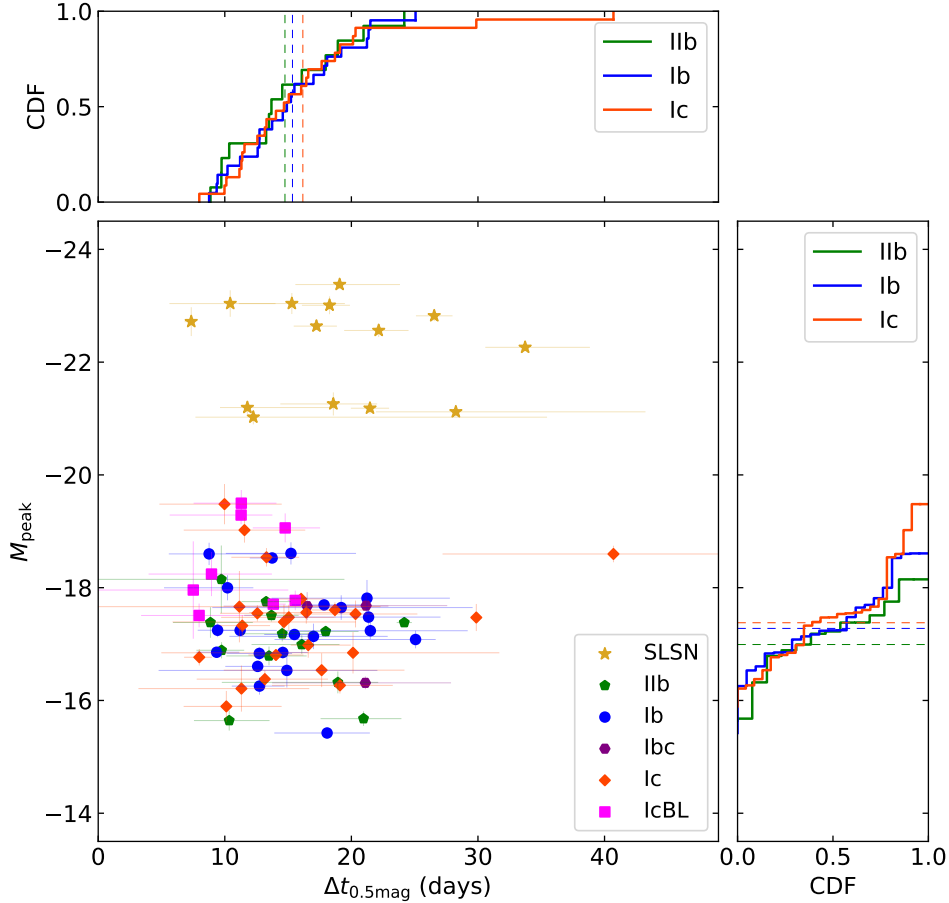


Figure 6. A relation between the decline timescales and the peak luminosity. The different colors show the different SN types of the SNe as shown in the legend. The dashed lines in the CDFs show the average.

have adopted $\Delta t_{0.5\text{mag}}$ to obtain the timescale mainly determined by the photon diffusion. For some of the light curves, $\Delta t_{1\text{mag}}$ is affected by the ^{56}Co tail.

First, we estimate the ejecta mass M_{ej} from the observed decline timescale $\Delta t_{0.5\text{mag}}$. For this purpose, we calculate a set of bolometric light curves using the semi-analytic model (Arnett 1982) based on the prescription by Chatzopoulos et al. (2012). To calculate the light curves, we need the ejecta velocity v_{ej} , optical opacity κ and gamma-ray opacity κ_{γ} , and the ejecta mass M_{ej} . In particular, $\Delta t_{0.5\text{mag}}$ is sensitive to the ejecta velocity, the opacity in the ejecta, and the ejecta mass as it reflects the diffusion timescale. For the ejecta velocity, we adopt a constant, typical velocity $v_{\text{ej}} = 10,000 \text{ km s}^{-1}$ ($\pm 2,000 \text{ km s}^{-1}$) (e.g., Lyman et al. 2016) as observations show relatively homogenous velocity (in Appendix A, we discuss the case when we fix the kinetic energy to $E_{\text{k}} = 10^{51} \text{ erg}$). It is noted that the variation of the velocity is not included in the error propagation. Even though the error causes $\sim 20\%$ uncertainty of the ejecta mass, this does not affect our conclusions (see Section

4.2). For the optical opacity, we use a constant opacity $\kappa = 0.07 \text{ cm}^2 \text{ g}^{-1}$ following previous studies (e.g., Cano 2013; Taddia et al. 2018), which can reproduce the light curves of SNe well when the dominant opacity source is electron scattering (e.g., Chevalier 1992). For the gamma-ray opacity, we assume $\kappa_{\gamma} = 0.03 \text{ cm}^2 \text{ g}^{-1}$ (Sutherland & Wheeler 1984). This choice does not affect our results because we mainly use the light curve around the peak. With these fixed parameters, we calculate bolometric light curves by varying the ejecta mass. Then, by matching the calculated $\Delta t_{0.5\text{mag}}$ and observed $\Delta t_{0.5\text{mag}}$, we derive the ejecta mass for each SN. An example of the light curve comparison is shown in Figure 7.

Next, we estimate the ^{56}Ni mass M_{Ni} from the peak magnitude (or the peak luminosity). The ^{56}Ni mass is estimated from the peak luminosity of the SN because the peak luminosity equals the instantaneous luminosity generated by the radioactive decay of ^{56}Ni and ^{56}Co (Arnett 1979) as shown in Figure 7. The radioactive decay luminosity is expressed as follows (Nadyozhin

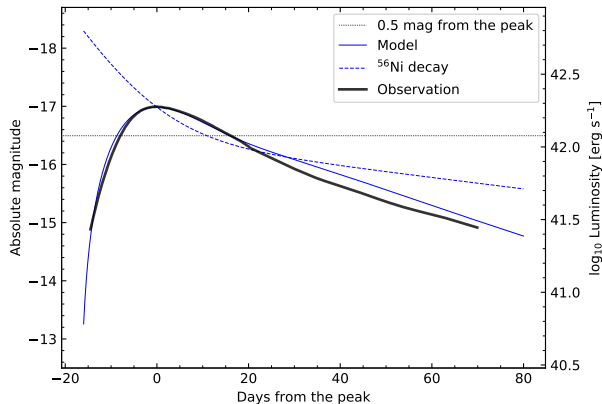


Figure 7. An example of the comparison between the bolometric light curve constructed by observations (the black solid line, Type IIb SN 2006T) and the corresponding semi-analytic model (the blue solid line) with the deposition by the radioactive decay of ^{56}Ni and ^{56}Co (the blue dashed line). The luminosity of the observation and the semi-analytic model coincide at their peaks and at the time when the magnitudes decline by 0.5 mag from the peaks (the black dotted line).

1994):

$$L(t) = (L_{\text{Ni}}e^{-t/\tau_{\text{Ni}}} + L_{\text{Co}}e^{-t/\tau_{\text{Co}}}) \left(\frac{M_{\text{Ni}}}{M_{\odot}} \right), \quad (1)$$

where the $L_{\text{Ni}} = 6.45 \times 10^{43} \text{ erg s}^{-1}$, $L_{\text{Co}} = 1.45 \times 10^{43} \text{ erg s}^{-1}$, $\tau_{\text{Ni}} = 8.8$ days, and $\tau_{\text{Co}} = 111.3$ days. Substituting the peak time t_{peak} and the peak luminosity $L(t_{\text{peak}})$ into Equation (1) provides the ^{56}Ni mass. The peak time t_{peak} is estimated from the decline timescale $\Delta t_{0.5\text{mag}}$ with an assumption that the relation between the decline timescale and the peak time follows that of the semi-analytic model (Arnett 1982; Chatzopoulos et al. 2012).

Figure 8 shows a relation between the ejecta masses M_{ej} and the synthesized ^{56}Ni masses M_{Ni} for 82 SNe estimated in the methods above (Table 6). Here, the derived ^{56}Ni masses have been divided by a correction factor of 1.4 since Dessart et al. (2016) has pointed out that the semi-analytic model (Arnett 1982) overestimates the ^{56}Ni by a factor of ~ 1.4 . It is noted that Khatami & Kasen (2019) and Afsariardchi et al. (2021) have suggested a factor of ~ 2 for the correction. Because the ^{56}Ni mass estimated from the method in Khatami & Kasen (2019) is consistent with that estimated from the tail of light curves, the ^{56}Ni mass can be considered as the lower limit of the ^{56}Ni mass. Thus, we divided

the ^{56}Ni mass estimated from the semi-analytic model (Arnett 1982) by a factor of 1.4.

The distribution of the ejecta masses is concentrated from $\sim 1 M_{\odot}$ to $\sim 4 M_{\odot}$ as shown in Figure 8. This result is consistent with previous studies (e.g., Drout et al. 2011; Cano 2013; Barbarino et al. 2021), supporting our assumptions for the estimate of the ejecta mass. From the distribution of the ejecta masses M_{ej} , pre-SN masses M_{preSN} are estimated to be $\sim 2.5 M_{\odot} - \sim 5.5 M_{\odot}$ with $M_{\text{preSN}} = M_{\text{ej}} + M_{\text{NS}}$, where M_{NS} the neutron star (NS) mass remaining after the SN explosion and the a typical NS mass is $\sim 1.4 M_{\odot}$ (Lattimer 2012). These relatively small masses of pre-SNe suggest that progenitor stars of almost all the SESNe originate from binary systems, as shown by previous studies (e.g., Eldridge et al. 2008; Yoon et al. 2010; Sana et al. 2012; Sravan et al. 2019). The distributions of M_{ej} and M_{Ni} do not depend on the SN types. P-values from K-S tests for Type IIb vs. Ib SNe, Type Ib vs. Ic SNe, and Type Ic vs. IIb SNe are summarized in Table 2.

The ^{56}Ni masses of almost all the SLSNe exceed the ejecta masses with the assumption that the heating source is the radioactive decay of ^{56}Ni even though it may not be the case. The large ^{56}Ni masses suggest that the SLSNe require energy sources other than the radioactive decay of ^{56}Ni . Furthermore, although the ^{56}Ni masses of many normal SNe are less than 10 % of the ejecta masses, some normal SNe show high ^{56}Ni masses, ~ 20 % of the ejecta masses. In Section 4, we discuss necessary conditions to reproduce the ^{56}Ni mass derived for normal SNe.

4. DISCUSSIONS

4.1. Hydrodynamics and nucleosynthesis calculations

In this section, we investigate what conditions of SN explosion can reproduce the relation between the ejecta mass and the synthesized ^{56}Ni mass by performing hydrodynamics and nucleosynthesis calculations. Since the synthesized ^{56}Ni mass depends not only on the explosion timescales but also on structures of progenitor stars, we take them into account to discuss the explosion timescales and synthesized ^{56}Ni masses. Finally, we compare results of the calculations with the observations.

4.1.1. Method of calculations

We employ a one-dimensional Lagrangian hydrodynamics calculation code, bcode (Morozova et al. 2015) and 21-isotopes nucleosynthesis ¹ in our calculations,

¹ http://cococubed.asu.edu/code_pages/burn_helium.shtml

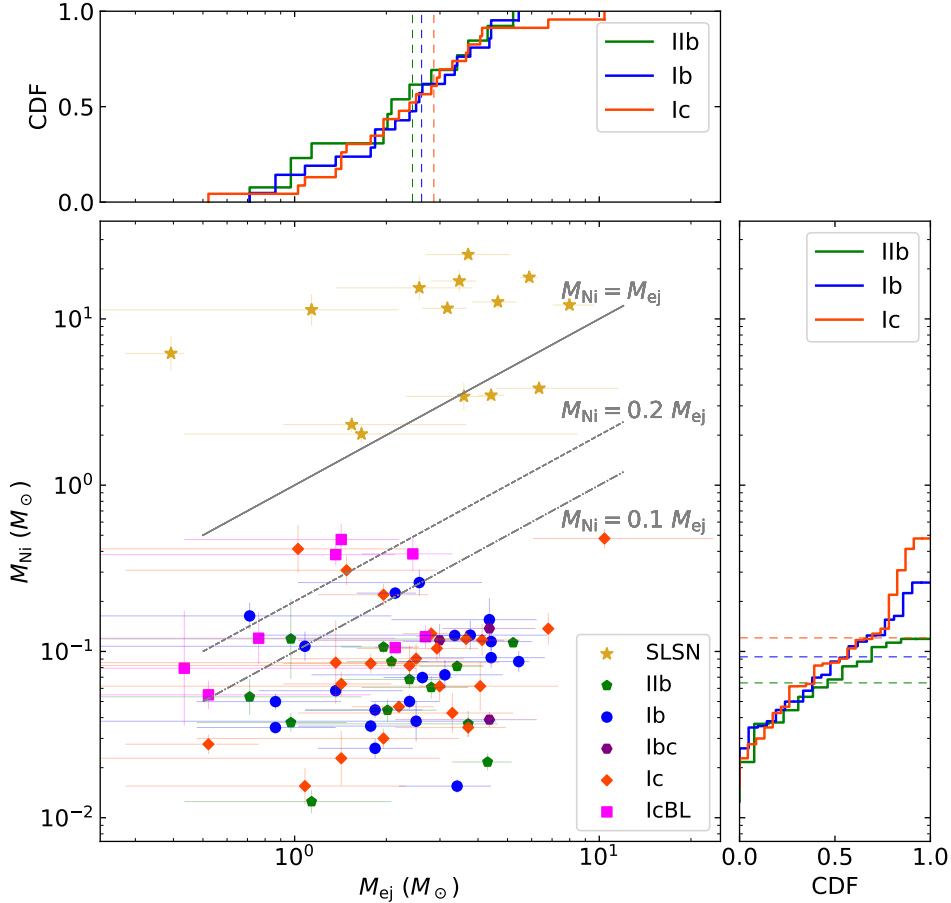


Figure 8. A comparison between ejecta masses and synthesized ^{56}Ni masses. The different colors show different SN types as shown in the legend. The gray lines represent $M_{\text{Ni}} = M_{\text{ej}}$, $M_{\text{Ni}} = 0.2 M_{\text{ej}}$, and $M_{\text{Ni}} = 0.1 M_{\text{ej}}$ from top to bottom. The dashed lines in the CDF show the average.

Table 1. P-values of the K-S test.

Types	IIb & Ib	Ib & Ic	Ic & IIb
$\Delta t_{0.5\text{mag}}$	0.91	1.00	0.90
M_{peak}	0.93	0.56	0.25

following the modeling of the explosion performed in [Sawada & Maeda \(2019\)](#). It is noted that production of ^{56}Ni is slightly overestimated in the case of 21-isotopes ([Timmes 1999](#)). However, this does not affect the final conclusions because we discuss the lower limit of the explosion timescale, that is, the upper limit of the ^{56}Ni mass. Thus, it is more conservative to consider the case that can synthesize more ^{56}Ni mass.

Table 2. P-values of the K-S test.

Types	IIb & Ib	Ib & Ic	Ic & IIb
M_{ej}	0.98	1.00	0.90
M_{Ni}	0.45	0.99	0.51

Basic equations of hydrodynamics to be solved are following:

$$\frac{\partial r}{\partial m} = \frac{1}{4\pi r^2 \rho} \quad (2)$$

$$\frac{Dv}{Dt} = -\frac{Gm}{r^2} - 4\pi r^2 \frac{\partial P}{\partial m} \quad (3)$$

$$\frac{D\epsilon}{Dt} = -P \frac{D}{Dt} \left(\frac{1}{\rho} \right) + \dot{\epsilon}_{\text{in}} \quad (4)$$

where $\dot{\epsilon}_{\text{in}}$ is the energy injection rate per mass. Here, the term of the energy generation by the nucleosynthesis is ignored because the energy is negligible compared with the energy injection $\dot{\epsilon}_{\text{in}}$ in this work. The energy

injection rate $\dot{\epsilon}_{\text{in}}$ is described as

$$\dot{\epsilon}_{\text{in}} = \frac{E_{\text{k}} - (E_{\text{bind}} + E_{\text{int}})}{t_{\text{grow}}} \frac{1}{\Delta M} \quad (5)$$

so that the SN ejecta finally expand with the kinetic energy E_{k} . Here, E_{bind} is a binding energy of a progenitor star, E_{int} is an internal energy of the progenitor, ΔM is a mass in each mesh ($\Delta M = (M_{\text{core}} - 1.4 M_{\odot})/N_{\text{grid}}$; see Section 4.1.2 for $M_{\text{core}}, N_{\text{grid}} = 1000$), and t_{grow} is a timescale of an explosion. The energy is injected just outside of the inner boundary. It is noted that all the models are assumed to always explode with the input energy even though some progenitors may directly collapse to black holes without explosion (e.g., MacFadyen & Woosley 1999; Ugliano et al. 2012; Ertl et al. 2020).

4.1.2. Parameters of calculations

We parameterize the ejecta mass M_{ej} , which is related to the mass of the progenitor star, and the explosion timescale t_{grow} , with which the ejecta reach the final kinetic energy E_{k} as shown in Equation 5. This is because the synthesized ^{56}Ni mass depends both on the structure of the progenitor star and the explosion timescale. For the determination of the progenitor star from the ejecta mass, we adopt stellar evolution models by Sukhbold et al. (2016). Note that these are single star models although most of SESNe are considered to originate from binary systems (e.g., Maund et al. 2004; Eldridge et al. 2008; Yoon et al. 2010; Sana et al. 2012; Sravan et al. 2019). The use of single star models is justified because the inner structures of the progenitors from single stars are similar to those from binary systems when their core masses are similar (e.g., Sukhbold et al. 2016; Vartanyan et al. 2021).

For the ejecta mass, $M_{\text{ej}} = 1 M_{\odot} - 10 M_{\odot}$ are used to cover the range of the ejecta masses estimated from the observations, with a step of $1 M_{\odot}$. The ejecta mass plus the NS mass provides the corresponding pre-SN mass M_{preSN} (namely the core mass M_{core}) from this equation ($M_{\text{preSN}} = M_{\text{core}} = M_{\text{ej}} + M_{\text{NS}}$). Here, a typical mass of the NS mass, $1.4 M_{\odot}$ is adopted (Lattimer 2012). The uncertainty of the ^{56}Ni mass due to the NS mass is discussed in Appendix B, but our conclusions are not affected by the NS mass. Since the core mass is discretized following a model with the mass resolution of the ZAMS masses ($1 M_{\odot}$), the model with the nearest core mass is selected. Here, two progenitor stars, the progenitors with He layer and without He layer, are used to consider Type Ib and Ic SNe, respectively. The parameters of the progenitors used in our calculations are summarized in Table 3.

For the explosion timescale, $t_{\text{grow}} = [0.01, 0.03, 0.1, 0.3, 1.0]$ sec are tested. The lower bound

approximately corresponds to a free fall time of a iron core, which represents a prompt explosion. The upper bound is set to be 1 sec because almost no ^{56}Ni is synthesized with $t_{\text{grow}} > 1$ sec.

With the explosion timescale, the ejecta reach the final kinetic energy E_{k} expressed as $E_{\text{k}} = (3/10)M_{\text{ej}}v_{\text{ej}}^2$. This expression assumes homologously expanding ejecta ($R = v_{\text{ej}}t$) with a uniform density ($\rho = 3M_{\text{ej}}/4\pi R^3$) even though the actual density has a structure. We here fixed a typical velocity ($v_{\text{ej}} = 10,000 \text{ km s}^{-1}$) as in the parameter estimation in Section 3.2. In Appendix A, we show the results fixing the kinetic energy to $E_{\text{k}} = 10^{51}$ erg.

4.1.3. Synthesized ^{56}Ni mass

Table 4 summarizes the synthesized ^{56}Ni mass for each progenitor model with the five explosion timescales. Figure 9 represents the ejecta mass and the ^{56}Ni mass with the explosion timescale of 0.1, 0.3, and 1.0 sec, showing a comparison with the compactness parameter ($\xi_{M=1.75M_{\odot}} = (M/M_{\odot})/(R(M)/1000 \text{ km})$, O'Connor & Ott 2011). We do not show the results of explosion timescale of 0.01 and 0.03 sec because the synthesized ^{56}Ni masses of these timescales are the almost same as those of 0.1 sec as shown in Table 4. Here, it should be noted that Figure 9 shows the amount of ^{56}Ni mass newly synthesized by explosive nucleosynthesis, which corresponds to the maximum ejectable amount of ^{56}Ni .

In Table 4 and Figure 9, three trends of the ^{56}Ni mass are seen: (1) the synthesized ^{56}Ni mass decreases with the increase of the explosion timescale, (2) the ^{56}Ni mass correlates with the compactness, and (3) the ^{56}Ni roughly increases with the increase of the ejecta mass. These trends of the ^{56}Ni mass can be explained as follows.

^{56}Ni is synthesized around the core of the progenitor stars at the temperature $T \gtrsim 5 \times 10^9 \text{ K}$ (e.g., Woosley et al. 2002; Seitenzahl et al. 2009) after the shock propagation. In the shocked region, the kinetic energy E_{k} is comparable to the internal energy E_{int} . Also, the region for ^{56}Ni production is hot enough to be radiation dominant. Thus, the radius R of the temperature at which ^{56}Ni is synthesized can be estimated as below:

$$E_{\text{k}} \simeq E_{\text{int}} \simeq E_{\text{rad}} = aT^4 \frac{4\pi}{3} R^3 \quad (6)$$

$$R \sim 4 \times 10^8 \text{ cm} \left(\frac{E_{\text{k}}}{10^{51} \text{ erg}} \right)^{1/3} \left(\frac{T}{5 \times 10^9 \text{ K}} \right)^{-4/3} \quad (7)$$

where E_{rad} is the radiation energy. Therefore, the synthesized ^{56}Ni mass is approximately determined by the mass enclosed in this radius.

Table 3. A summary of progenitor star models

Model	$M_{\text{ZAMS}} (M_{\odot})$	$E_{\text{bind}} (10^{51} \text{ erg})$	$E_{\text{int}} (10^{51} \text{ erg})$	$E_{\text{k}} (10^{51} \text{ erg})$
He 1	10	-5.25	4.62	0.6
He 2	13	-5.32	4.58	1.2
He 3	15	-5.72	5.17	1.8
He 4	18	-5.88	5.29	2.4
He 5	20	-6.26	5.58	3.0
He 6	23	-7.48	6.66	3.6
He 7	25	-7.74	6.89	4.2
He 8	28	-8.23	7.35	4.8
He 9	30	-7.62	6.76	5.4
He 10	32	-8.14	7.19	6.0
CO 1	13	-5.40	3.91	0.6
CO 2	16	-5.63	4.02	1.2
CO 3	19	-5.95	3.86	1.8
CO 4	21	-5.96	3.96	2.4
CO 5	24	-8.04	3.67	3.0
CO 6	26	-7.49	3.70	3.6
CO 7	28	-8.51	4.00	4.2
CO 8	31	-8.02	3.76	4.8
CO 9	33	-8.74	3.65	5.4
CO 10	35	-9.63	3.62	6.0

The first trend that the decrease of the ^{56}Ni mass with the increase of the explosion timescale also shown in previous studies (e.g., Sawada & Maeda 2019) is interpreted as follows. The radius in Equation 7 is estimated for the case of the prompt explosion. In the case of a slow explosion, the SN starts to expand adiabatically due to the energy obtained initially. This causes the decrease of the internal energy, which in turn reduces the radius above. As a result, the amount of the synthesized ^{56}Ni decreases with the explosion timescale. Explosion with the timescales less than 0.1 sec shows almost constant ^{56}Ni masses. This is due to the timescale of the shockwave propagation. It takes ~ 0.4 sec for the shockwave to propagate the radius where the ^{56}Ni is synthesized ($R \lesssim 4 \times 10^8$ cm) with the shock velocity of $v_{\text{sh}} = 10,000$ km s^{-1} . Therefore, when the explosion timescale t_{grow} is considerably shorter than this timescale, the explosion is considered to be prompt, producing the almost constant ^{56}Ni masses.

Second, the variation of the ^{56}Ni mass with the ejecta mass follows the compactness of the core. In the cases of the higher compactness, the mass where ^{56}Ni is synthesized ($R \lesssim 4 \times 10^8$ cm) increases. This enhances the synthesized ^{56}Ni mass.

Third, there is an overall trend that the ^{56}Ni mass roughly increases with the increase of the ejecta mass. This is because the kinetic energy is assumed to be proportional to the ejecta mass in our calculations. For the

fixed kinetic energy ($E_{\text{k}} = 10^{51}$ erg), this overall trend of the ^{56}Ni mass with the increase of the ejecta mass is reduced (see Appendix A).

Our results give the highest luminosity for ^{56}Ni -powered SNe since the synthesized ^{56}Ni mass is the maximum ejectable amount of ^{56}Ni . No model except for the models of the CO core with the ejecta mass of $1 M_{\odot}$ and with the explosion timescale of 0.01 and 0.03 sec synthesize $M_{\text{Ni}} > 0.2 M_{\text{ej}}$. Even though the inner boundary is changed to $M = 1.2 M_{\odot}$, only the models of the CO core with the ejecta mass of $1 M_{\odot}$ and with the explosion timescale of ≤ 0.1 sec can synthesize $M_{\text{Ni}} \gtrsim 0.2 M_{\text{ej}}$ (see Appendix B). This indicates that the maximum luminosity that normal SNe powered by ^{56}Ni can reach is expressed as $M_{\text{Ni}} \lesssim 0.2 M_{\text{ej}}$. The objects with the ^{56}Ni mass exceeding this limit would suggest the existence of other power sources.

4.2. Constraints to the explosion timescale

Finally, we compare our results of the calculations with the observations to give constraints on the explosion timescale. Figure 10 shows a relation between the ejecta masses and the synthesized ^{56}Ni masses estimated from both the observations and the calculations. Since the ^{56}Ni masses are almost constant when the explosion timescales are less than 0.1 sec (see Section 4.1.3), we only show the results for $t_{\text{grow}} = 0.1, 0.3,$ and 1.0 sec in Figure 10. The observational results of Type

Table 4. Summary of the synthesized ^{56}Ni masses (in M_{\odot}) for each progenitor model and explosion timescale, t_{grow} .

Model	t_{grow} (s)				
	0.01	0.03	0.1	0.3	1.0
He 1	0.048	0.044	0.036	0.017	0.002
He 2	0.237	0.235	0.205	0.103	0.062
He 3	0.254	0.249	0.222	0.120	0.068
He 4	0.232	0.229	0.211	0.106	0.060
He 5	0.404	0.400	0.381	0.227	0.115
He 6	0.689	0.677	0.659	0.432	0.241
He 7	0.555	0.548	0.534	0.346	0.169
He 8	0.530	0.533	0.523	0.373	0.206
He 9	0.456	0.461	0.467	0.314	0.152
He 10	0.508	0.512	0.522	0.350	0.160
CO 1	0.215	0.210	0.166	0.081	0.061
CO 2	0.179	0.175	0.148	0.057	0.050
CO 3	0.285	0.281	0.267	0.143	0.081
CO 4	0.166	0.163	0.146	0.072	0.045
CO 5	0.656	0.642	0.622	0.404	0.240
CO 6	0.324	0.326	0.316	0.174	0.058
CO 7	0.518	0.519	0.507	0.354	0.198
CO 8	0.422	0.430	0.430	0.276	0.127
CO 9	0.547	0.545	0.550	0.368	0.171
CO 10	0.672	0.674	0.665	0.470	0.230

I Ib and Ib SNe (Type Ib-like SNe) and Type Ic and Ic-BL SNe (Type Ic-like SNe) are compared to the results of the progenitor models of the He core and the CO core, respectively. There are 34 Type Ib-like SNe and 31 Type Ic-like SNe in the diagrams. The SLSNe are excluded from the sample since their luminosity cannot be reproduced by the radioactive decay of ^{56}Ni .

In Figure 10, when the ^{56}Ni masses of the observed SNe are below the calculated ^{56}Ni masses, the observed SNe can be explained by the calculations. This is because the synthesized ^{56}Ni mass is the upper limit of the ejected ^{56}Ni mass with the SN ejecta as already mentioned in Section 4.1.3. As shown in Figure 10, the ^{56}Ni masses of almost all the observed SNe can be explained in the cases of $t_{\text{grow}} = 0.1$ sec. On the other hand, with $t_{\text{grow}} = 1.0$ sec, ^{56}Ni masses of more than half of the SNe are not reproduced. This result is not affected by the uncertainties of the ejecta masses even though we include additional 20 % error caused by the uncertainty of the ejecta velocity (Section 3.2).

Here, we discuss three systematic uncertainties in our analysis. First, we consider the accuracy of the ^{56}Ni mass estimated from the semi-analytic model (Arnett 1982). In Arnett’s rule, the distribution of the heating source is assumed to be the same as that of the density and the temperature. This is known to cause overestimate of the ^{56}Ni mass especially in cases of longer

timescales of light curves (e.g., Khatami & Kasen 2019). As mentioned in Section 3.2, the ^{56}Ni masses shown in Figure 8 are already divided by a factor of 1.4 to account for the effect. This has relaxed the condition of the explosion timescale t_{grow} , i.e., the longer timescale is acceptable.

Second, we have ignored the extinction of host galaxies, as mentioned in Section 2.3. If the extinction is $A_V \sim 0.6$ for Type IIb and Ib SNe, $A_V \sim 1$ for Type Ic SNe (Stritzinger et al. 2018), or $A_V \sim 0.9$ for SESNe (Zheng et al. 2022), the actual synthesized ^{56}Ni masses are larger by a factor of ~ 1.7 , ~ 2.5 , or ~ 2.3 , respectively. This requires even shorter explosion timescales t_{grow} . Therefore, ignoring extinction of host galaxies results in an underestimation of ^{56}Ni mass, and thus gives a conservative constraint to the explosion timescale t_{grow} .

Third, we change the way to select the sample objects. Since more luminous objects are detectable at larger distances, we limit the distance of the samples to remove the observational bias. We adopt the luminosity distance of $d_L = 100$ Mpc as the threshold. The numbers of Type Ib-like and Type Ic-like SNe within $d_L = 100$ Mpc decreased to 29 and 27, respectively. Figure 11 shows this relation. Again, this gives conservative constraints to the explosion timescale t_{grow} .

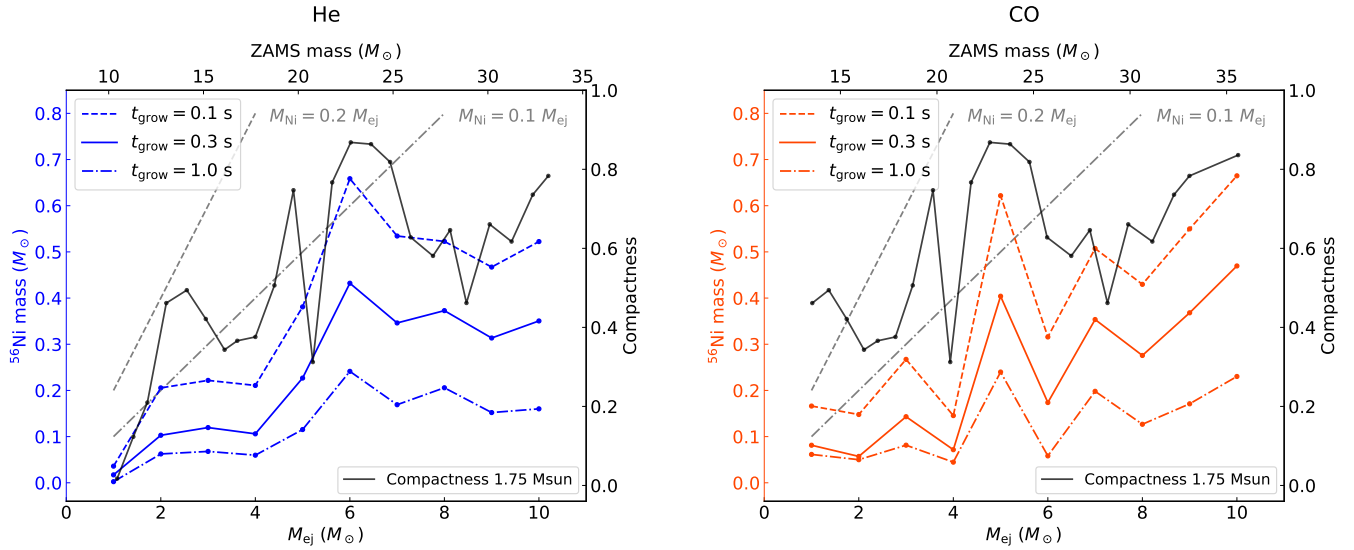


Figure 9. A relation between the ejecta mass and the synthesized ^{56}Ni mass calculated with the various explosion timescales. Left panel: results from He cores. Right panel: results from CO cores. The different types of the colored lines show the different explosion timescales as shown in the legend. The black lines show compactness at $1.75 M_{\odot}$ in mass coordinate. The dashed-dotted and dashed gray lines are the lines showing $M_{\text{Ni}} = 0.1 M_{\text{ej}}$ and $M_{\text{ej}} = 0.2 M_{\text{ej}}$, respectively.

Figure 12 summarizes fractions that the synthesized ^{56}Ni masses can be explained by each explosion timescale for all the sample and for the volume-limited sample. Here, we note that we excluded the SNe with the ejecta mass of $< 1 M_{\odot}$ or $> 10 M_{\odot}$ because the progenitor models of our calculations do not cover the mass range. The fraction that the ^{56}Ni mass can be explained by our calculations increases by $\sim 5\%$ from all the sample to the volume-limited sample since the number of SNe with larger ^{56}Ni mass decreased. The synthesized ^{56}Ni mass from our calculations of the explosions with the timescale of 1.0 sec (“slow” explosions preferred by ab-initio calculations) cannot explain the ^{56}Ni mass of 50 % of SNe in the volume-limited sample.

To explain ^{56}Ni mass of the majority of SNe even in the volume-limited sample, the explosion timescale should be shorter than 0.3 sec. As discussed above, we have divided the ^{56}Ni mass by 1.4 (Section 3.2) and ignored the host extinction (Section 2.3) to give conservative estimate of ^{56}Ni mass. Besides, the calculated ^{56}Ni mass is slightly overestimated since we have adopted 21-isotopes nucleosynthesis (Section 4.1.1). Moreover, the calculated ^{56}Ni mass is the upper limit (Section 4.1.3) as the entire ^{56}Ni is not necessarily ejected. Therefore, we conclude that majority of CCSNe need to explode with the timescale of $t_{\text{grow}} < 0.3$

sec. This conclusion is consistent with Sawada & Maeda (2019), which suggested “rapid” explosion ($t_{\text{grow}} \lesssim 0.25$ sec) for normal Type II SNe. Also, our conclusions are in line with those by Sollerman et al. (2021), which has shown that many SESNe show higher luminosity than that in the models with calibrated-neutrino luminosity.

Note that our calculations are based on one-dimensional artificial explosion, and much simpler than ab-initio calculations with the neutrino-driven mechanism (e.g., Janka 2012) and models with calibrated neutrino luminosity (e.g., Ugliano et al. 2012; Ertl et al. 2020; Woosley et al. 2021). Nevertheless, our results give a constraint to the explosion timescale of CCSNe in a model-independent manner: in order to explain the synthesized ^{56}Ni mass in the majority of the observed SESNe, any mechanisms which corresponds to the one-dimensional calculation with $t_{\text{grow}} < 0.3$ sec is preferable.

It is also noted that even the rapid explosions with 0.1 sec cannot reproduce the ^{56}Ni masses of some SNe. There are several possibilities to produce additional ^{56}Ni . If some SNe explode by leaving a NS with small ejecta mass and eject material from a deeper core, more ^{56}Ni can be ejected. Although such a case is likely to be a minority according to the observed NS mass distribution (Lattimer 2012), our calculations with an inner boundary of $1.2 M_{\odot}$ show that additional $\sim 0.1 M_{\odot}$ of

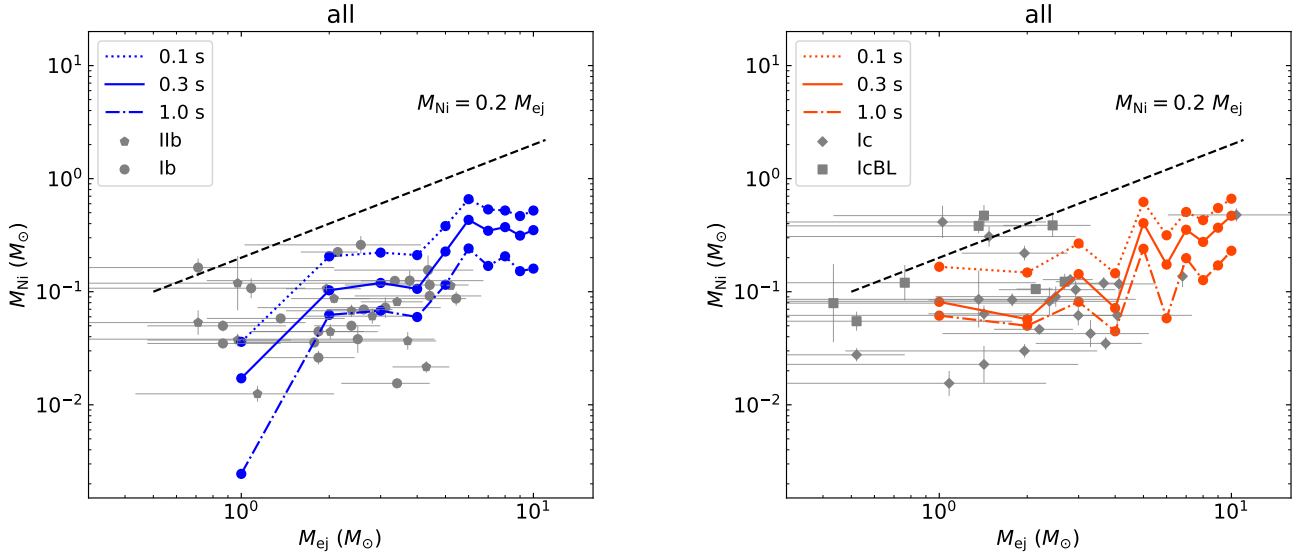


Figure 10. A comparison of the ejecta masses and the synthesized ^{56}Ni masses. The gray dots represent the observations, and the colored solid, dashed and dashed-and-dotted lines show results of the calculations with explosion timescales of 0.1 sec, 0.3 sec and 1.0 sec, respectively. The black dashed line shows a condition where $M_{\text{Ni}} = 0.2 M_{\text{ej}}$. Left panel: Type IIb and Type Ib SNe with the calculations using the progenitor models of the He cores. Right panel: Type Ic and Type Ic BL SNe with the calculations using the progenitor models of the CO cores.

^{56}Ni can be ejected as compared with the case with the inner boundary of $1.4 M_{\odot}$ (see Appendix B). Another mechanism that additionally produces ^{56}Ni is neutrino-driven wind after the explosive synthesis (e.g., Wongwathanarat et al. 2017; Wanajo et al. 2018; Sawada & Suwa 2021), which can increase $\lesssim 0.05 M_{\odot}$ of ^{56}Ni . As discussed in Section 4.1.3, it is difficult to explain the luminosity of SNe with $M_{\text{Ni}} > 0.2 M_{\text{ej}}$ by the radioactive decay of ^{56}Ni . Such SNe may be regarded as a category of SLSNe, which would require other power sources, such as magnetars (e.g., Kasen & Bildsten 2010; Woosley 2010; Mösta et al. 2014).

Constraints on the explosion timescale will be reinforced by future observations. Although our calculations show the overall trend that the ^{56}Ni mass correlates with the ejecta mass as mentioned in Section 4.1.3, the observational results do not seem to show the clear trend. This is because of the small sample size for high ejecta mass ($\gtrsim 5 M_{\odot}$). When more SNe with high ejecta mass are discovered in future observations, we can test

the trend with the ejecta mass and the relation between ^{56}Ni production and the progenitor structure.

5. SUMMARY

In this work, we focus on ^{56}Ni to give constraints on the explosion timescale of CCSNe. We perform systematic analysis of multi-band light curves of 82 SESNe (including SLSNe-I) to obtain bolometric light curves, which is one of the largest sample numbers among the research regarding bolometric light curves of SESNe based on multi-band SEDs. We measure the decline timescale $\Delta t_{0.5\text{mag}}$ of the light curves and the peak magnitude M_{peak} . There is no clear correlation between them, which is consistent with previous studies. Also, the distributions of these parameters are similar among Type IIb, Ib, and Ic SNe. Then, we estimate the ejecta mass and the ^{56}Ni mass from the decline timescale and the peak magnitude using the semi-analytic model (Arnett 1982; Chatzopoulos et al. 2012).

We carry out one-dimensional hydrodynamics and nucleosynthesis calculations, varying the progenitor mass

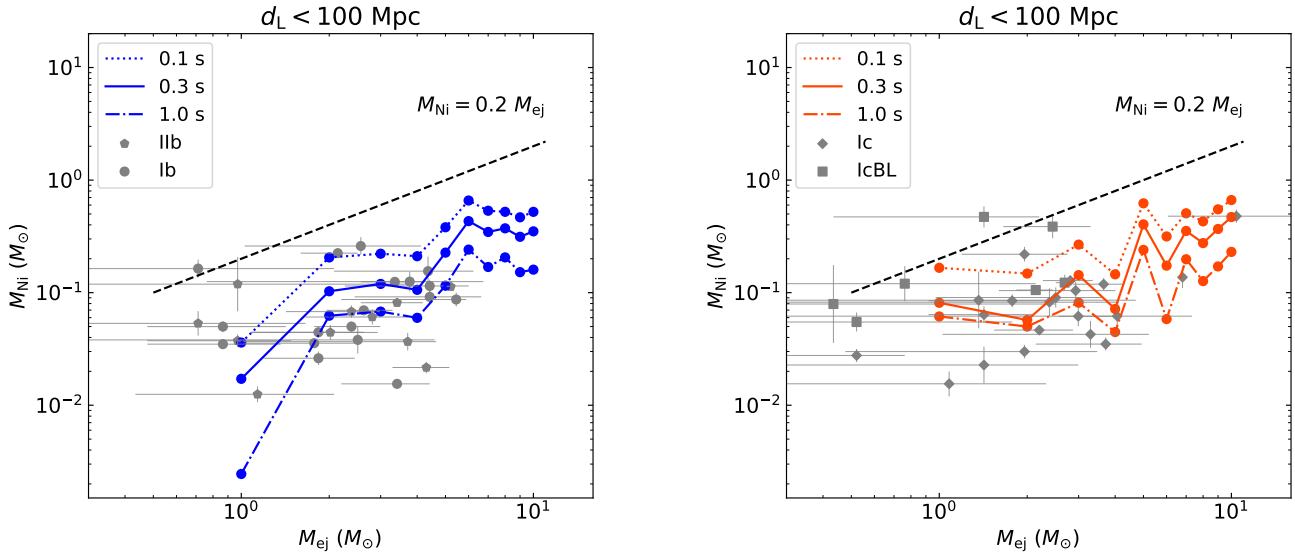


Figure 11. Same as Figure 10 but for the volume-limited sample within 100 Mpc.

and the explosion timescale to evaluate the ^{56}Ni mass. We find that the synthesized ^{56}Ni mass is less than $\sim 0.2 M_{\text{ej}}$, showing that the maximum luminosity of normal CCSNe powered by ^{56}Ni is determined by $M_{\text{Ni}} \lesssim 0.2 M_{\text{ej}}$. This suggests that SNe exceeding the upper limit of the ^{56}Ni mass are likely to have other power sources.

From the comparison of the ^{56}Ni mass estimated from the observations and the calculations, we find that the explosions with 1.0 sec (slow explosions preferred by *ab-initio* calculations) can only explain less than 50 % of the ^{56}Ni mass of the SNe, and the explosions with 0.3 sec can explain the majority of ^{56}Ni mass of the SNe in

our sample. Therefore, we conclude that the explosion timescale of CCSNe is shorter than 0.3 sec to explain the ^{56}Ni mass of the majority of SESNe.

- 1 This work was supported by JSPS KAKENHI
- 2 Grant Number JP21J22515 and Graduate Program
- 3 on Physics for the Universe (GP-PU), Tohoku Uni-
- 4 versity (S.S.); JSPS KAKENHI Grant Number
- 5 JP17H06363, JP19H00694, JP20H00158, JP20H00179,
- 6 and JP21H04997 (M.T.); JP21J00825 and JP21K13964
- 7 (R.S.); JP18K13585, JP20H00174, JP21K13966, and
- 8 JP21H04997 (T.M.).

REFERENCES

- Afsariardchi, N., Drout, M. R., Khatami, D. K., et al. 2021, *ApJ*, 918, 89
- Anderson, J. P. 2019, *A&A*, 628, A7
- Arcavi, I., Wolf, W. M., Howell, D. A., Bildsten, L., & PTF, S. 2016, in *American Astronomical Society Meeting Abstracts*, Vol. 227, American Astronomical Society Meeting Abstracts #227, 208.02
- Arnett, W. D. 1966, *Canadian Journal of Physics*, 44, 2553
- . 1979, *ApJL*, 230, L37
- . 1982, *ApJ*, 253, 785
- Barbarino, C., Sollerman, J., Taddia, F., et al. 2021, *A&A*, 651, A81
- Bethe, H. A., & Wilson, J. R. 1985, *ApJ*, 295, 14
- Blanton, M. R., & Roweis, S. 2007, *AJ*, 133, 734
- Bollig, R., Yadav, N., Kresse, D., et al. 2021, *ApJ*, 915, 28

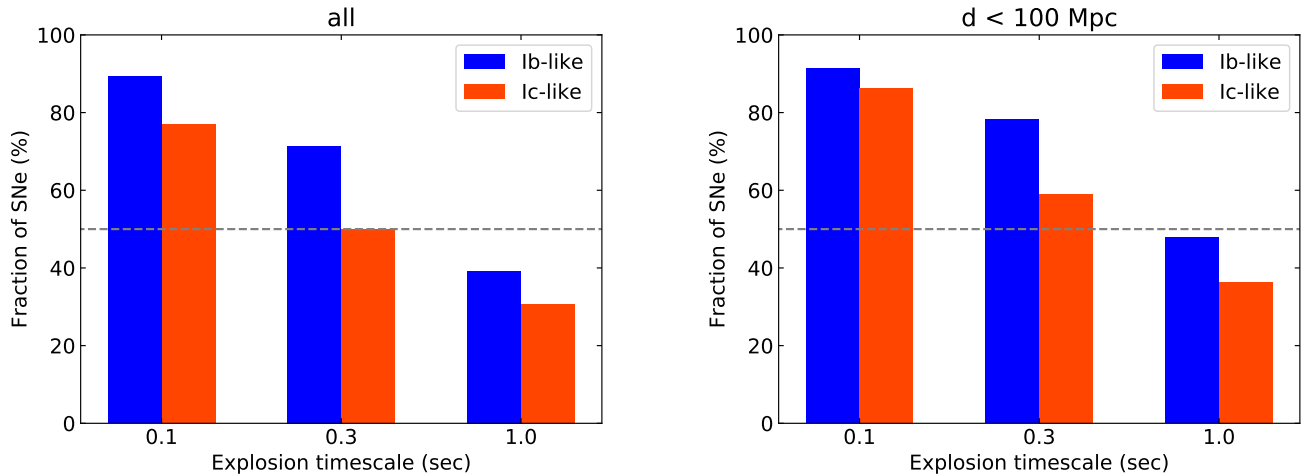


Figure 12. Fractions of SNe whose ^{56}Ni mass can be explained with each explosion timescale. The blue and red colors show Type Ib-like (IIb and Ib) and Type Ic-like (Ic and Ic BL) SNe, respectively. Left: all the sample. Right: volume-limited sample within 100 Mpc. The horizontal gray dashed lines show 50 % fraction.

Burrows, A., Radice, D., & Vartanyan, D. 2019, MNRAS, 485, 3153
 Burrows, A., Radice, D., Vartanyan, D., et al. 2020, MNRAS, 491, 2715
 Burrows, A., & Vartanyan, D. 2021, Nature, 589, 29
 Cano, Z. 2013, MNRAS, 434, 1098
 Chatzopoulos, E., Wheeler, J. C., & Vinko, J. 2012, ApJ, 746, 121
 Chevalier, R. A. 1992, ApJ, 394, 599
 Colgate, S. A., & White, R. H. 1966, ApJ, 143, 626
 De Cia, A., Gal-Yam, A., Rubin, A., et al. 2018, ApJ, 860, 100
 Dessart, L., Hillier, D. J., Woosley, S., et al. 2016, MNRAS, 458, 1618
 Drout, M. R., Soderberg, A. M., Gal-Yam, A., et al. 2011, ApJ, 741, 97
 Eldridge, J. J., Izzard, R. G., & Tout, C. A. 2008, MNRAS, 384, 1109
 Ertl, T., Woosley, S. E., Sukhbold, T., & Janka, H. T. 2020, ApJ, 890, 51
 Gal-Yam, A. 2012, Science, 337, 927

Guillochon, J., Parrent, J., Kelley, L. Z., & Margutti, R. 2017, ApJ, 835, 64
 Hamuy, M. 2003, ApJ, 582, 905
 Janka, H.-T. 2012, Annual Review of Nuclear and Particle Science, 62, 407
 Kasen, D., & Bildsten, L. 2010, ApJ, 717, 245
 Khatami, D. K., & Kasen, D. N. 2019, ApJ, 878, 56
 Lattimer, J. M. 2012, Annual Review of Nuclear and Particle Science, 62, 485
 Lentz, E. J., Bruenn, S. W., Hix, W. R., et al. 2015, ApJL, 807, L31
 Lyman, J. D., Bersier, D., James, P. A., et al. 2016, MNRAS, 457, 328
 MacFadyen, A. I., & Woosley, S. E. 1999, ApJ, 524, 262
 Maeda, K., & Tominaga, N. 2009, MNRAS, 394, 1317
 Maund, J. R., Smartt, S. J., Kudritzki, R. P., Podsiadlowski, P., & Gilmore, G. F. 2004, Nature, 427, 129
 Melson, T., Janka, H.-T., Bollig, R., et al. 2015a, ApJL, 808, L42
 Melson, T., Janka, H.-T., & Marek, A. 2015b, ApJL, 801, L24

- Meza, N., & Anderson, J. P. 2020, *A&A*, 641, A177
- Modjaz, M., Li, W., Butler, N., et al. 2009, *ApJ*, 702, 226
- Moriya, T. J., Sorokina, E. I., & Chevalier, R. A. 2018, *SSRv*, 214, 59
- Morozova, V., Ott, C. D., & Piro, A. L. 2015, *SNEC: SuperNova Explosion Code*, , , ascl:1505.033
- Mösta, P., Richers, S., Ott, C. D., et al. 2014, *ApJL*, 785, L29
- Müller, B., Melson, T., Heger, A., & Janka, H.-T. 2017, *MNRAS*, 472, 491
- Müller, B., Tauris, T. M., Heger, A., et al. 2019, *MNRAS*, 484, 3307
- Nadyozhin, D. K. 1994, *ApJS*, 92, 527
- Nicholl, M. 2021, arXiv e-prints, arXiv:2109.08697
- O'Connor, E., & Ott, C. D. 2011, *ApJ*, 730, 70
- Ott, C. D., Roberts, L. F., da Silva Schneider, A., et al. 2018, *ApJL*, 855, L3
- Ouchi, R., Maeda, K., Anderson, J. P., & Sawada, R. 2021, arXiv e-prints, arXiv:2109.00603
- Pejcha, O., & Prieto, J. L. 2015, *ApJ*, 806, 225
- Perley, D. A., Fremling, C., Sollerman, J., et al. 2020, *ApJ*, 904, 35
- Prentice, S. J., Inserra, C., Schulze, S., et al. 2021, *MNRAS*, arXiv:2109.14572
- Sana, H., de Mink, S. E., de Koter, A., et al. 2012, *Science*, 337, 444
- Sawada, R., & Maeda, K. 2019, *ApJ*, 886, 47
- Sawada, R., & Suwa, Y. 2021, *ApJ*, 908, 6
- Schlegel, D. J., Finkbeiner, D. P., & Davis, M. 1998, *ApJ*, 500, 525
- Seitenzahl, I. R., Townsley, D. M., Peng, F., & Truran, J. W. 2009, *Atomic Data and Nuclear Data Tables*, 95, 96
- Sollerman, J., Yang, S., Perley, D., et al. 2021, arXiv e-prints, arXiv:2109.14339
- Sravan, N., Marchant, P., & Kalogera, V. 2019, *ApJ*, 885, 130
- Stockinger, G., Janka, H. T., Kresse, D., et al. 2020, *MNRAS*, 496, 2039
- Stritzinger, M. D., Taddia, F., Burns, C. R., et al. 2018, *A&A*, 609, A135
- Sukhbold, T., Ertl, T., Woosley, S. E., Brown, J. M., & Janka, H. T. 2016, *ApJ*, 821, 38
- Summa, A., Janka, H.-T., Melson, T., & Marek, A. 2018, *ApJ*, 852, 28
- Sutherland, P. G., & Wheeler, J. C. 1984, *ApJ*, 280, 282
- Suwa, Y., & Tominaga, N. 2015, *MNRAS*, 451, 282
- Suwa, Y., Tominaga, N., & Maeda, K. 2019, *MNRAS*, 483, 3607
- Taddia, F., Sollerman, J., Leloudas, G., et al. 2015, *A&A*, 574, A60
- Taddia, F., Stritzinger, M. D., Bersten, M., et al. 2018, *A&A*, 609, A136
- Takiwaki, T., Kotake, K., & Suwa, Y. 2014, *ApJ*, 786, 83
- Timmes, F. X. 1999, *ApJS*, 124, 241
- Tully, R. B., & Fisher, J. R. 1977, *A&A*, 500, 105
- Ugliano, M., Janka, H.-T., Marek, A., & Arcones, A. 2012, *ApJ*, 757, 69
- Vartanyan, D., Laplace, E., Renzo, M., et al. 2021, arXiv e-prints, arXiv:2104.03317
- Wanajo, S., Müller, B., Janka, H.-T., & Heger, A. 2018, *ApJ*, 852, 40
- Wongwathanarat, A., Janka, H.-T., Müller, E., Pllumbi, E., & Wanajo, S. 2017, *ApJ*, 842, 13
- Woosley, S. E. 1988, *ApJ*, 330, 218
- . 2010, *ApJL*, 719, L204
- Woosley, S. E., Heger, A., & Weaver, T. A. 2002, *Reviews of Modern Physics*, 74, 1015
- Woosley, S. E., Sukhbold, T., & Kasen, D. N. 2021, *ApJ*, 913, 145
- Woosley, S. E., & Weaver, T. A. 1995, *ApJS*, 101, 181
- Yoon, S. C., Woosley, S. E., & Langer, N. 2010, *ApJ*, 725, 940
- Zheng, W., Stahl, B. E., de Jaeger, T., et al. 2022, *MNRAS*, arXiv:2203.05596

APPENDIX A: M_{ej} VS. M_{Ni} FROM A CONSTANT KINETIC ENERGY

In this Appendix, we show results of parameter estimation and nucleosynthesis by adopting a constant kinetic energy $E_k = 10^{51}$ erg. Figure 13 represents a relation between the ejecta mass and the ^{56}Ni mass. The ejecta masses estimated from calculations are concentrated on $\sim 1 M_\odot$ to $\sim 2 M_\odot$ in contrast to the case that the kinetic energy is proportional to the ejecta mass with the constant velocity $v_{\text{ej}} = 10,000 \text{ km s}^{-1}$ (Figure 10). This is because the ejecta velocity is observationally estimated to concentrate around $v_{\text{ej}} = 10,000 \text{ km s}^{-1}$ (e.g., Lyman et al. 2016), and then the typical ejecta mass becomes $\sim (5/3) M_\odot$ from the relation of $E_k = (3/10)M_{\text{ej}}v_{\text{ej}}^2$. We here emphasize that the case that the kinetic energy is proportional to the ejecta mass assumed in the main text is more realistic as shown in previous studies (e.g., Taddia et al. 2018). All the ^{56}Ni masses except for the case of $M_{\text{ej}} = 1 M_\odot$ are lower than those in the case of the constant ejecta velocity (Figure 10) because the kinetic energy $E_k = 10^{51}$ erg is higher only when the ejecta mass is $1 M_\odot$. The fraction that the ^{56}Ni mass estimated from the observations can be explained by the calculations with each explosion timescale is almost same as the case of the kinetic energy proportional to the ejecta mass. This does not affect our conclusions on the explosion timescale of CCSNe.

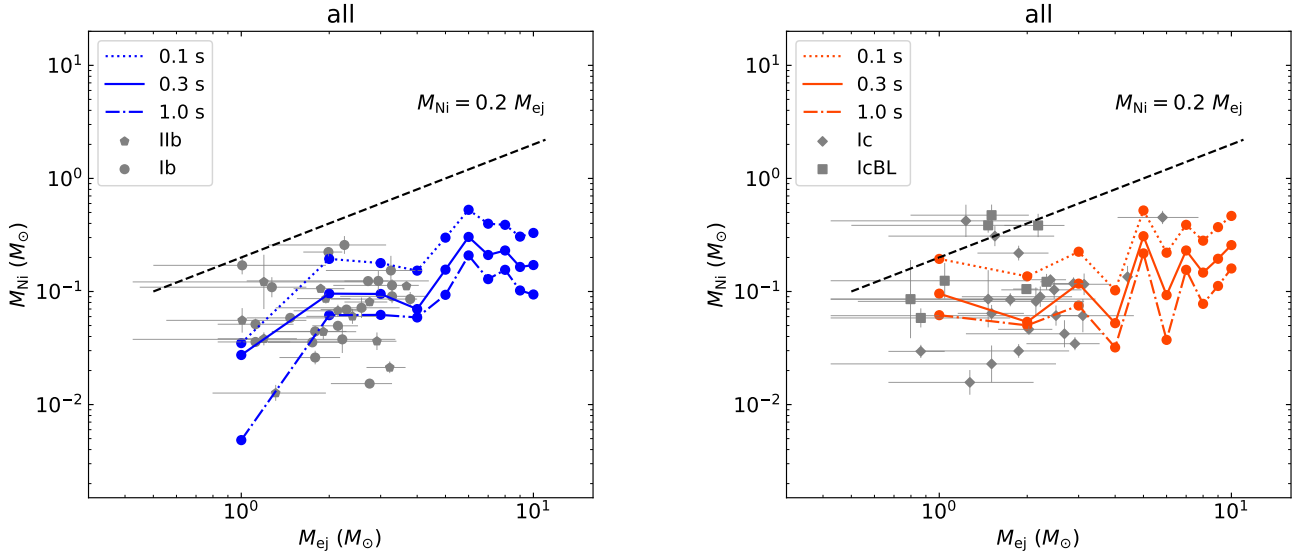


Figure 13. Same as Figure 10 but the kinetic energy used for the estimate of the ejecta mass and used in the calculations are fixed to $E_k = 10^{51}$ erg.

APPENDIX B: INNER BOUNDARY

Here, we show the results of the calculations by changing the inner boundary of the calculations from $1.4 M_\odot$ to $1.2 M_\odot$. In the calculations, we just change the inner boundary where the energy is input, keeping the progenitor model and the injection energy the same. Table 5 summarizes the synthesized ^{56}Ni mass. The ^{56}Ni masses with the boundary of $1.2 M_\odot$ are $\sim 0.05 - 0.1 M_\odot$ higher than the cases with $1.4 M_\odot$ as shown in Figure 14. Not all the material enclosed in $1.2 - 1.4 M_\odot$ in a mass coordinate becomes ^{56}Ni because a large part of the innermost material becomes ^{56}Fe due to the low electron fraction ($Y_e \sim 0.46$).

Table 5. Summary of the synthesized ^{56}Ni masses (in M_{\odot}) for each progenitor model and explosion timescale, t_{grow} .

Model	t_{grow} (s)				
	0.01	0.03	0.1	0.3	1.0
He 1	0.179	0.176	0.142	0.092	0.079
He 2	0.339	0.328	0.299	0.176	0.132
He 3	0.360	0.355	0.337	0.203	0.141
He 4	0.325	0.318	0.307	0.184	0.113
He 5	0.482	0.468	0.447	0.276	0.156
He 6	0.761	0.746	0.722	0.489	0.286
He 7	0.626	0.617	0.596	0.400	0.212
He 8	0.613	0.613	0.602	0.441	0.247
He 9	0.530	0.528	0.516	0.360	0.185
He 10	0.581	0.578	0.565	0.397	0.197
CO 1	0.315	0.306	0.266	0.160	0.133
CO 2	0.260	0.252	0.218	0.114	0.078
CO 3	0.367	0.355	0.329	0.184	0.127
CO 4	0.238	0.235	0.221	0.101	0.049
CO 5	0.728	0.710	0.685	0.459	0.282
CO 6	0.399	0.391	0.374	0.227	0.099
CO 7	0.597	0.595	0.585	0.418	0.240
CO 8	0.493	0.490	0.478	0.321	0.161
CO 9	0.620	0.614	0.598	0.415	0.209
CO 10	0.751	0.741	0.722	0.522	0.273

Figure 15 shows the comparison of the results of the inner boundary of $1.2 M_{\odot}$ with the volume-limited sample of the observations. The models with the inner boundary $1.2 M_{\odot}$ can explain the ^{56}Ni mass of some SNe that cannot be explained by the models with the inner boundary $1.4 M_{\odot}$. This suggests that SNe with higher ^{56}Ni masses may leave NSs with smaller masses. It is, however, noted that such an explosion is likely to be a minority since many of NSs are known from observations to have $\sim 1.4 M_{\odot}$ (Lattimer 2012).

APPENDIX C

We summarize information and derived physical parameters for all the SNe in our final sample in Table 6.

Table 6. A summary of properties of all the samples.

Name	Type	d_L (Mpc)	$\Delta t_{0.5\text{mag}}$ (days)	M_{peak} (mag)	M_{ej} (M_{\odot})	M_{Ni} (M_{\odot})
SN 1962L	Ic	15.2	$11.2^{+11.2}_{-11.2}$	$-17.66^{+0.63}_{-0.63}$	$1.36^{+3.34}_{-1.31}$	$0.12^{+0.09}_{-0.05}$
SN 1994I	Ic	7.8	$8.0^{+1.0}_{-1.2}$	$-16.77^{+0.15}_{-0.15}$	$0.52^{+0.24}_{-0.24}$	$0.039^{+0.006}_{-0.005}$
SN 1996cb	IIb	17.0	$24.2^{+0.6}_{-0.6}$	$-17.38^{+0.06}_{-0.06}$	$5.22^{+0.17}_{-0.17}$	$0.16^{+0.01}_{-0.01}$
SN 1997ef	Ic BL	52.2	$7.5^{+7.5}_{-7.5}$	$-17.96^{+0.86}_{-0.86}$	$0.43^{+2.07}_{-0.38}$	$0.11^{+0.13}_{-0.06}$
SN 1998bw	Ic BL	37.9	$11.3^{+2.8}_{-3.8}$	$-19.50^{+0.23}_{-0.23}$	$1.42^{+0.78}_{-0.99}$	$0.66^{+0.16}_{-0.13}$
SN 1999ex	Ic	41.0	$14.0^{+2.2}_{-2.2}$	$-16.81^{+0.08}_{-0.08}$	$2.20^{+0.67}_{-0.66}$	$0.065^{+0.005}_{-0.005}$
SN 2002ap	Ic BL	9.3	$15.6^{+0.6}_{-0.6}$	$-17.77^{+0.17}_{-0.17}$	$2.69^{+0.18}_{-0.18}$	$0.17^{+0.03}_{-0.03}$
SN 2003bg	Ic	20.2	$29.9^{+0.2}_{-0.4}$	$-17.47^{+0.24}_{-0.24}$	$6.80^{+0.06}_{-0.12}$	$0.19^{+0.05}_{-0.04}$
SN 2003id	Ic	32.6	$11.3^{+5.4}_{-8.1}$	$-16.21^{+0.41}_{-0.41}$	$1.42^{+1.57}_{-1.36}$	$0.032^{+0.015}_{-0.010}$

Table 6 continued

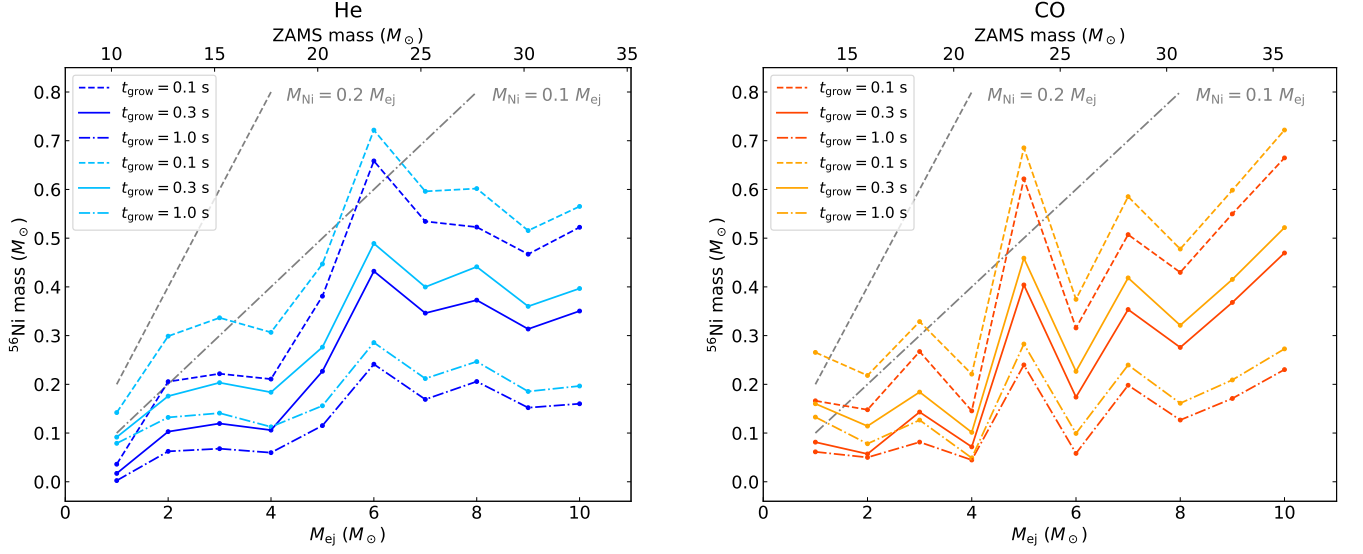


Figure 14. A relation between the ejecta mass and the ^{56}Ni mass. The light blue lines and the orange lines are the results of the inner boundary of $1.2 M_{\odot}$ in the left and right panels, respectively.

Table 6 (continued)

Name	Type	d_L (Mpc)	$\Delta t_{0.5\text{mag}}$ (days)	M_{peak} (mag)	M_{ej} (M_{\odot})	M_{Ni} (M_{\odot})
SN 2004aw	Ic	71.7	$18.7^{+2.4}_{-2.6}$	$-17.60^{+0.14}_{-0.14}$	$3.65^{+0.65}_{-0.78}$	$0.17^{+0.02}_{-0.02}$
SN 2004dk	Ib	20.0	$25.1^{+1.6}_{-11.1}$	$-17.08^{+0.16}_{-0.16}$	$5.44^{+0.45}_{-3.24}$	$0.12^{+0.02}_{-0.02}$
SN 2004dn	Ic	56.3	$16.6^{+3.4}_{-1.4}$	$-16.98^{+0.22}_{-0.22}$	$2.99^{+1.02}_{-0.43}$	$0.086^{+0.020}_{-0.016}$
SN 2004ex	IIb	80.8	$14.5^{+2.6}_{-3.1}$	$-17.18^{+0.14}_{-0.14}$	$2.38^{+0.73}_{-0.96}$	$0.095^{+0.013}_{-0.011}$
SN 2004fe	Ic	80.8	$12.6^{+2.6}_{-2.9}$	$-17.55^{+0.14}_{-0.14}$	$1.78^{+0.79}_{-0.86}$	$0.12^{+0.02}_{-0.01}$
SN 2004ff	IIb	104.0	$13.7^{+2.2}_{-2.2}$	$-17.51^{+0.11}_{-0.11}$	$2.08^{+0.67}_{-0.60}$	$0.12^{+0.01}_{-0.01}$
SN 2004gq	Ib	28.2	$15.5^{+2.2}_{-2.4}$	$-17.17^{+0.10}_{-0.10}$	$2.63^{+0.67}_{-0.67}$	$0.098^{+0.009}_{-0.008}$
SN 2004gt	Ic	18.1	$19.1^{+4.2}_{-5.4}$	$-16.27^{+0.14}_{-0.14}$	$3.71^{+1.22}_{-1.57}$	$0.049^{+0.007}_{-0.006}$
SN 2004gv	Ib	90.0	$17.8^{+2.9}_{-2.5}$	$-17.69^{+0.09}_{-0.09}$	$3.35^{+0.89}_{-0.79}$	$0.17^{+0.02}_{-0.01}$
SN 2005aw	Ic	42.3	$15.1^{+3.6}_{-5.3}$	$-17.47^{+0.23}_{-0.23}$	$2.50^{+1.09}_{-1.53}$	$0.13^{+0.03}_{-0.02}$
SN 2005az	Ic	33.0	$17.6^{+6.5}_{-7.7}$	$-16.54^{+0.30}_{-0.30}$	$3.29^{+1.92}_{-2.27}$	$0.060^{+0.019}_{-0.014}$
SN 2005bf	Ib	84.9	$13.7^{+1.2}_{-1.8}$	$-18.53^{+0.09}_{-0.09}$	$2.14^{+0.37}_{-0.54}$	$0.31^{+0.03}_{-0.03}$
SN 2005bj	Ic	99.0	$16.4^{+3.5}_{-4.5}$	$-17.56^{+0.20}_{-0.20}$	$2.93^{+1.08}_{-1.33}$	$0.15^{+0.03}_{-0.02}$
SN 2005em	IIb	113.5	$13.3^{+2.0}_{-2.0}$	$-17.75^{+0.09}_{-0.09}$	$1.96^{+0.61}_{-0.54}$	$0.15^{+0.01}_{-0.01}$
SN 2005hg	Ib	94.4	$19.2^{+10.4}_{-10.2}$	$-17.65^{+0.22}_{-0.22}$	$3.77^{+2.97}_{-3.01}$	$0.18^{+0.04}_{-0.03}$
SN 2005hl	Ib	104.4	$17.0^{+5.9}_{-6.6}$	$-17.14^{+0.23}_{-0.23}$	$3.11^{+1.70}_{-1.98}$	$0.10^{+0.02}_{-0.02}$
SN 2005hm	Ib	158.0	$11.2^{+2.9}_{-2.1}$	$-17.24^{+0.05}_{-0.05}$	$1.36^{+0.90}_{-0.60}$	$0.081^{+0.004}_{-0.004}$
SN 2005kl	Ic	22.2	$20.1^{+11.6}_{-15.1}$	$-16.85^{+0.37}_{-0.37}$	$4.07^{+3.26}_{-4.01}$	$0.087^{+0.035}_{-0.025}$
SN 2005kr	Ic BL	650.1	$11.3^{+2.5}_{-5.6}$	$-19.29^{+0.16}_{-0.16}$	$1.36^{+0.78}_{-1.26}$	$0.54^{+0.09}_{-0.07}$
SN 2006T	IIb	31.0	$16.1^{+3.0}_{-4.0}$	$-16.99^{+0.17}_{-0.17}$	$2.81^{+0.90}_{-1.15}$	$0.085^{+0.014}_{-0.012}$

Table 6 continued

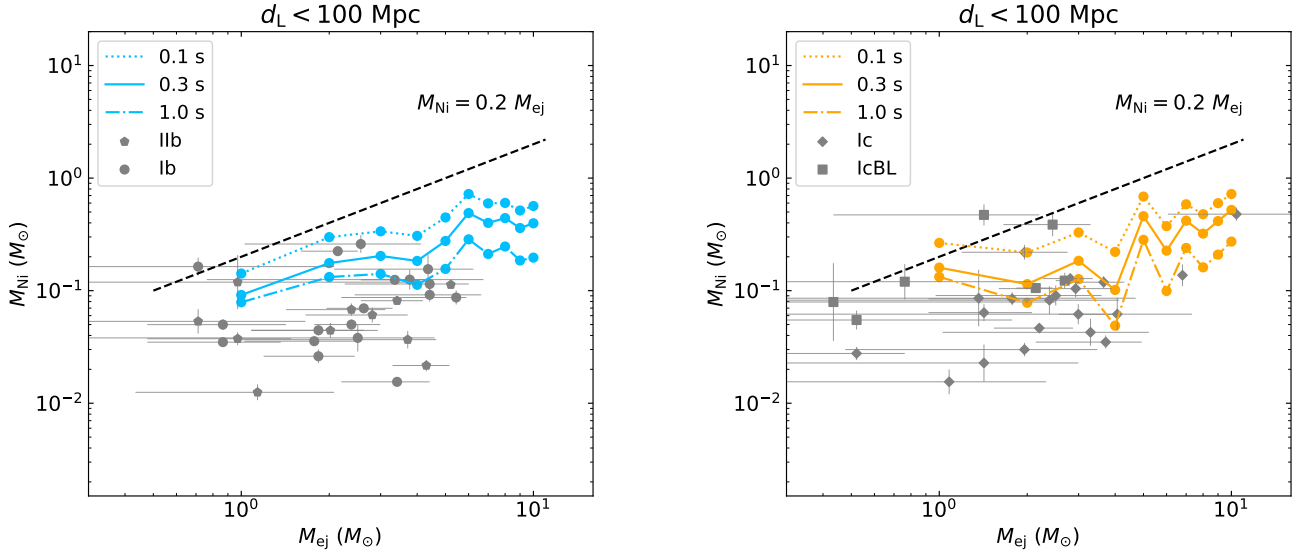


Figure 15. Same as Figure 10 but the inner boundary in the calculations is changed to $1.2 M_{\odot}$.

Table 6 (continued)

Name	Type	d_L (Mpc)	$\Delta t_{0.5\text{mag}}$ (days)	M_{peak} (mag)	M_{ej} (M_{\odot})	M_{Ni} (M_{\odot})
SN 2006ep	Ib	63.0	$14.6^{+2.0}_{-2.0}$	$-16.85^{+0.11}_{-0.11}$	$2.38^{+0.61}_{-0.61}$	$0.070^{+0.007}_{-0.007}$
SN 2006fo	Ib	93.1	$21.4^{+5.7}_{-7.2}$	$-17.48^{+0.14}_{-0.14}$	$4.42^{+1.59}_{-2.16}$	$0.16^{+0.02}_{-0.02}$
SN 2006jo	Ib	360.0	$10.2^{+2.0}_{-5.0}$	$-18.00^{+0.22}_{-0.22}$	$1.08^{+0.58}_{-1.01}$	$0.15^{+0.03}_{-0.03}$
SN 2006lc	Ib	59.0	$12.6^{+2.2}_{-2.6}$	$-16.60^{+0.10}_{-0.10}$	$1.78^{+0.67}_{-0.75}$	$0.050^{+0.005}_{-0.004}$
SN 2006nx	Ic	603.9	$11.6^{+4.8}_{-4.8}$	$-19.02^{+0.22}_{-0.22}$	$1.48^{+1.45}_{-1.20}$	$0.43^{+0.10}_{-0.08}$
SN 2007C	Ib	29.0	$12.7^{+2.6}_{-2.6}$	$-16.83^{+0.12}_{-0.12}$	$1.84^{+0.79}_{-0.76}$	$0.062^{+0.007}_{-0.006}$
SN 2007Y	Ib	19.3	$12.7^{+2.0}_{-2.2}$	$-16.25^{+0.15}_{-0.15}$	$1.84^{+0.61}_{-0.64}$	$0.037^{+0.005}_{-0.005}$
SN 2007ay	IIb	67.1	$8.9^{+3.3}_{-3.0}$	$-17.38^{+0.27}_{-0.27}$	$0.71^{+0.95}_{-0.56}$	$0.075^{+0.021}_{-0.016}$
SN 2007cl	Ic	99.9	$14.7^{+5.7}_{-8.8}$	$-17.39^{+0.31}_{-0.31}$	$2.38^{+1.74}_{-2.25}$	$0.12^{+0.04}_{-0.03}$
SN 2007gr	Ic	10.0	$11.4^{+2.2}_{-1.8}$	$-17.33^{+0.19}_{-0.19}$	$1.42^{+0.66}_{-0.50}$	$0.089^{+0.017}_{-0.014}$
SN 2007hn	Ib/c	140.0	$21.2^{+6.4}_{-4.3}$	$-17.68^{+0.19}_{-0.19}$	$4.36^{+1.82}_{-1.31}$	$0.19^{+0.04}_{-0.03}$
SN 2007kj	Ib	80.3	$9.4^{+2.0}_{-1.6}$	$-17.25^{+0.12}_{-0.12}$	$0.87^{+0.56}_{-0.39}$	$0.070^{+0.008}_{-0.007}$
SN 2007ru	Ic BL	69.4	$14.8^{+2.8}_{-2.6}$	$-19.06^{+0.26}_{-0.26}$	$2.44^{+0.85}_{-0.79}$	$0.54^{+0.14}_{-0.11}$
SN 2007uy	Ib	27.0	$14.9^{+7.2}_{-10.1}$	$-16.53^{+0.30}_{-0.30}$	$2.50^{+2.08}_{-2.45}$	$0.053^{+0.017}_{-0.013}$
SN 2008D	Ib	27.0	$18.1^{+3.4}_{-4.2}$	$-15.42^{+0.10}_{-0.10}$	$3.41^{+1.00}_{-1.21}$	$0.022^{+0.002}_{-0.002}$

Table 6 continued

Table 6 (continued)

Name	Type	d_L (Mpc)	$\Delta t_{0.5\text{mag}}$ (days)	M_{peak} (mag)	M_{ej} (M_{\odot})	M_{Ni} (M_{\odot})
SN 2008aq	I Ib	32.8	$13.5^{+3.0}_{-3.4}$	$-16.79^{+0.17}_{-0.17}$	$2.02^{+0.91}_{-0.94}$	$0.062^{+0.010}_{-0.009}$
SN 2008ax	I Ib	6.5	$21.0^{+3.0}_{-3.4}$	$-15.68^{+0.13}_{-0.13}$	$4.30^{+0.86}_{-1.01}$	$0.030^{+0.004}_{-0.003}$
SN 2008bo	I Ib	21.0	$10.3^{+3.2}_{-2.8}$	$-15.64^{+0.18}_{-0.18}$	$1.14^{+0.94}_{-0.70}$	$0.018^{+0.003}_{-0.003}$
SN 2009bb	Ic	46.4	$16.0^{+1.8}_{-1.8}$	$-17.80^{+0.11}_{-0.11}$	$2.81^{+0.54}_{-0.55}$	$0.18^{+0.02}_{-0.02}$
SN 2009dp	Ic	104.5	$20.3^{+4.9}_{-4.9}$	$-17.53^{+0.24}_{-0.24}$	$4.13^{+1.37}_{-1.50}$	$0.16^{+0.04}_{-0.03}$
SN 2009iz	Ib	62.6	$21.5^{+7.7}_{-6.7}$	$-17.24^{+0.15}_{-0.15}$	$4.42^{+2.21}_{-1.97}$	$0.13^{+0.02}_{-0.02}$
SN 2009jf	Ib	31.0	$21.2^{+6.5}_{-7.5}$	$-17.81^{+0.32}_{-0.32}$	$4.36^{+1.87}_{-2.28}$	$0.22^{+0.08}_{-0.06}$
SN 2009mg	I Ib	37.0	$9.7^{+9.7}_{-9.7}$	$-18.15^{+0.60}_{-0.60}$	$0.97^{+2.86}_{-0.91}$	$0.17^{+0.12}_{-0.07}$
PTF09cnd	SLSN-I	1349.8	$19.1^{+4.8}_{-3.5}$	$-23.38^{+0.08}_{-0.08}$	$3.71^{+1.39}_{-1.03}$	$34.12^{+2.56}_{-2.38}$
SN 2010md	SLSN-I	468.8	$18.6^{+3.5}_{-4.2}$	$-21.26^{+0.20}_{-0.20}$	$3.59^{+1.00}_{-1.27}$	$4.79^{+0.99}_{-0.82}$
PS1-10awh	SLSN-I	6031.0	$15.3^{+4.2}_{-4.2}$	$-23.04^{+0.19}_{-0.19}$	$2.57^{+1.27}_{-1.20}$	$21.52^{+4.02}_{-3.39}$
PS1-10ky	SLSN-I	6425.0	$10.4^{+3.6}_{-4.8}$	$-23.04^{+0.24}_{-0.24}$	$1.14^{+1.06}_{-1.03}$	$15.88^{+3.84}_{-3.09}$
SN 2011bm	Ic	99.0	$40.7^{+11.5}_{-13.5}$	$-18.60^{+0.15}_{-0.15}$	$10.40^{+13.27}_{-4.34}$	$0.67^{+0.10}_{-0.08}$
SN 2011dh	I Ib	8.0	$18.0^{+2.6}_{-2.8}$	$-17.22^{+0.09}_{-0.09}$	$3.41^{+0.77}_{-0.85}$	$0.11^{+0.01}_{-0.01}$
SN 2011hs	I Ib	30.3	$9.7^{+1.8}_{-2.0}$	$-16.89^{+0.14}_{-0.14}$	$0.97^{+0.51}_{-0.50}$	$0.052^{+0.007}_{-0.006}$
SN 2011ke	SLSN-I	697.8	$7.4^{+0.2}_{-0.5}$	$-22.72^{+0.26}_{-0.26}$	$0.39^{+0.04}_{-0.11}$	$8.69^{+2.31}_{-1.82}$
SN 2011kg	SLSN-I	968.7	$21.5^{+1.5}_{-1.5}$	$-21.18^{+0.09}_{-0.09}$	$4.42^{+0.46}_{-0.41}$	$4.87^{+0.44}_{-0.41}$
PS1-11ap	SLSN-I	3087.0	$33.7^{+5.1}_{-3.1}$	$-22.26^{+0.06}_{-0.06}$	$7.98^{+1.63}_{-0.95}$	$16.97^{+1.00}_{-0.94}$
SN 2012P	Ib/c	27.4	$21.1^{+6.8}_{-7.4}$	$-16.31^{+0.11}_{-0.11}$	$4.36^{+1.87}_{-2.22}$	$0.054^{+0.006}_{-0.005}$
SN 2012ap	Ic BL	54.7	$13.8^{+1.0}_{-1.0}$	$-17.71^{+0.09}_{-0.09}$	$2.14^{+0.30}_{-0.30}$	$0.15^{+0.01}_{-0.01}$
SN 2012au	Ib	23.6	$8.8^{+4.8}_{-3.2}$	$-18.60^{+0.20}_{-0.20}$	$0.71^{+1.37}_{-0.60}$	$0.23^{+0.05}_{-0.04}$
SN 2012bz	Ic	1498.0	$10.0^{+4.5}_{-5.1}$	$-19.48^{+0.36}_{-0.36}$	$1.03^{+1.30}_{-0.97}$	$0.58^{+0.23}_{-0.16}$
SN 2012hn	Ic	33.8	$10.1^{+4.4}_{-3.4}$	$-15.89^{+0.27}_{-0.27}$	$1.08^{+1.24}_{-0.80}$	$0.022^{+0.006}_{-0.005}$
PS1-12bqf	SLSN-I	3073.0	$28.3^{+15.0}_{-6.3}$	$-21.12^{+0.08}_{-0.08}$	$6.34^{+5.24}_{-1.76}$	$5.36^{+0.41}_{-0.38}$
PTF12dam	SLSN-I	512.5	$26.5^{+1.4}_{-1.4}$	$-22.82^{+0.09}_{-0.09}$	$5.89^{+0.40}_{-0.39}$	$24.90^{+2.21}_{-2.03}$
SN 2013ak	I Ib	7.0	$18.9^{+3.2}_{-9.2}$	$-16.32^{+0.19}_{-0.19}$	$3.71^{+0.93}_{-2.74}$	$0.051^{+0.010}_{-0.008}$
SN 2013hy	SLSN-I	4103.0	$11.8^{+7.1}_{-2.2}$	$-21.20^{+0.11}_{-0.11}$	$1.54^{+2.11}_{-0.62}$	$3.24^{+0.35}_{-0.32}$
iPTF13ajg	SLSN-I	4690.0	$18.3^{+1.6}_{-2.2}$	$-23.01^{+0.16}_{-0.16}$	$3.47^{+0.48}_{-0.67}$	$23.66^{+3.71}_{-3.21}$
iPTF13bvn	Ib	22.5	$9.4^{+1.8}_{-1.6}$	$-16.86^{+0.09}_{-0.09}$	$0.87^{+0.50}_{-0.39}$	$0.049^{+0.004}_{-0.004}$
SN 2014L	Ic	35.8	$13.3^{+2.6}_{-2.8}$	$-18.54^{+0.16}_{-0.16}$	$1.96^{+0.79}_{-0.76}$	$0.31^{+0.05}_{-0.04}$
SN 2014ad	Ic BL	25.3	$8.9^{+4.8}_{-5.0}$	$-18.24^{+0.39}_{-0.39}$	$0.76^{+1.38}_{-0.70}$	$0.17^{+0.07}_{-0.05}$
SN 2015ap	Ib	50.8	$15.2^{+5.1}_{-5.1}$	$-18.61^{+0.20}_{-0.20}$	$2.57^{+1.56}_{-1.54}$	$0.36^{+0.07}_{-0.06}$
SN 2015bn	SLSN-I	544.8	$17.2^{+1.6}_{-1.8}$	$-22.64^{+0.06}_{-0.06}$	$3.17^{+0.48}_{-0.55}$	$16.22^{+1.00}_{-0.94}$
SN 2016coi	Ic BL	16.2	$8.0^{+4.6}_{-4.6}$	$-17.51^{+0.21}_{-0.21}$	$0.52^{+1.26}_{-0.46}$	$0.077^{+0.016}_{-0.014}$
SN 2016eay	SLSN-I	481.9	$22.2^{+2.4}_{-2.7}$	$-22.56^{+0.12}_{-0.12}$	$4.65^{+0.68}_{-0.82}$	$17.71^{+2.00}_{-1.80}$
PS16yj	SLSN-I	1148.0	$12.3^{+23.2}_{-4.6}$	$-21.02^{+0.13}_{-0.13}$	$1.66^{+6.82}_{-1.22}$	$2.84^{+0.35}_{-0.31}$
SN 2017ein	Ic	17.0	$13.2^{+5.0}_{-5.4}$	$-16.38^{+0.15}_{-0.15}$	$1.96^{+1.52}_{-1.48}$	$0.042^{+0.006}_{-0.005}$
DES17C1ffz	Ib/c	427.5	$16.5^{+6.4}_{-6.6}$	$-17.67^{+0.25}_{-0.25}$	$2.99^{+1.88}_{-1.97}$	$0.16^{+0.04}_{-0.03}$